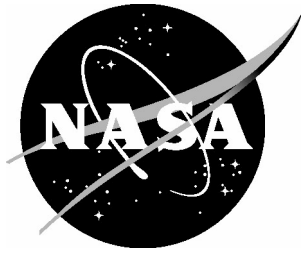


NASA/TP-2005-213784



Verification and Validation: High Charge and Energy (HZE) Transport Codes and Future Development

*John W. Wilson, Ram K. Tripathi, Christopher J. Mertens, Steve R. Blattmig, and Martha S. Cloudsley
Langley Research Center, Hampton, Virginia*

*Francis A. Cucinotta
Johnson Space Center, Houston, Texas*

*John Tweed, John H. Heinbockel, Steven A. Walker, and John E. Nealy
Old Dominion University, Norfolk, Virginia*

The NASA STI Program Office . . . in Profile

Since its founding, NASA has been dedicated to the advancement of aeronautics and space science. The NASA Scientific and Technical Information (STI) Program Office plays a key part in helping NASA maintain this important role.

The NASA STI Program Office is operated by Langley Research Center, the lead center for NASA's scientific and technical information. The NASA STI Program Office provides access to the NASA STI Database, the largest collection of aeronautical and space science STI in the world. The Program Office is also NASA's institutional mechanism for disseminating the results of its research and development activities. These results are published by NASA in the NASA STI Report Series, which includes the following report types:

- **TECHNICAL PUBLICATION.** Reports of completed research or a major significant phase of research that present the results of NASA programs and include extensive data or theoretical analysis. Includes compilations of significant scientific and technical data and information deemed to be of continuing reference value. NASA counterpart of peer-reviewed formal professional papers, but having less stringent limitations on manuscript length and extent of graphic presentations.
- **TECHNICAL MEMORANDUM.** Scientific and technical findings that are preliminary or of specialized interest, e.g., quick release reports, working papers, and bibliographies that contain minimal annotation. Does not contain extensive analysis.
- **CONTRACTOR REPORT.** Scientific and technical findings by NASA-sponsored contractors and grantees.

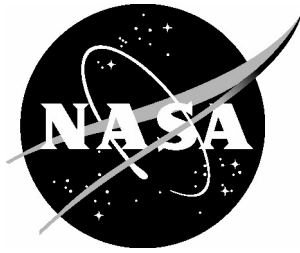
- **CONFERENCE PUBLICATION.** Collected papers from scientific and technical conferences, symposia, seminars, or other meetings sponsored or co-sponsored by NASA.
- **SPECIAL PUBLICATION.** Scientific, technical, or historical information from NASA programs, projects, and missions, often concerned with subjects having substantial public interest.
- **TECHNICAL TRANSLATION.** English-language translations of foreign scientific and technical material pertinent to NASA's mission.

Specialized services that complement the STI Program Office's diverse offerings include creating custom thesauri, building customized databases, organizing and publishing research results ... even providing videos.

For more information about the NASA STI Program Office, see the following:

- Access the NASA STI Program Home Page at <http://www.sti.nasa.gov>
- E-mail your question via the Internet to help@sti.nasa.gov
- Fax your question to the NASA STI Help Desk at (301) 621-0134
- Phone the NASA STI Help Desk at (301) 621-0390
- Write to:
NASA STI Help Desk
NASA Center for AeroSpace Information
7121 Standard Drive
Hanover, MD 21076-1320

NASA/TP-2005-213784



Verification and Validation: High Charge and Energy (HZE) Transport Codes and Future Development

*John W. Wilson, Ram K. Tripathi, Christopher J. Mertens, Steve R. Blattnig, and
Martha S. Cloudsley
Langley Research Center, Hampton, Virginia*

*Francis A. Cucinotta
Johnson Space Center, Houston, Texas*

*John Tweed, John H. Heinbockel, Steven A. Walker, and John E. Nealy
Old Dominion University, Norfolk, Virginia*

National Aeronautics and
Space Administration

Langley Research Center
Hampton, Virginia 23681-2199

July 2005

Available from:

NASA Center for AeroSpace Information (CASI)
7121 Standard Drive
Hanover, MD 21076-1320
(301) 621-0390

National Technical Information Service (NTIS)
5285 Port Royal Road
Springfield, VA 22161-2171
(703) 605-6000

Verification and Validation: High Charge and Energy (HZE) Transport Codes and Future Development

J.W. Wilson, R.K. Tripathi, C.J. Mertens, S. Blattnig, M.S. Cloudsley
NASA Langley Research Center

F. A. Cucinotta
NASA Johnson Space Center

and

J. Tweed, J. H. Heinbockel, S.A. Walker, J.E. Nealy
Old Dominion University

ABSTRACT

In the present paper, we give the formalism for further developing a fully three-dimensional HZETRN code using marching procedures but also development of a new Green's function code is discussed. The final Green's function code is capable of not only validation in the space environment but also in ground based laboratories with directed beams of ions of specific energy and characterized with detailed diagnostic particle spectrometer devices. Special emphasis is given to verification of the computational procedures and validation of the resultant computational model using laboratory and spaceflight measurements. Due to historical requirements, two parallel development paths for computational model implementation using marching procedures and Green's function techniques are followed. A new version of the HZETRN code capable of simulating HZE ions with either laboratory or space boundary conditions is under development. Validation of computational models at this time is particularly important for President Bush's Initiative to develop infrastructure for human exploration with first target demonstration of the Crew Exploration Vehicle (CEV) in low Earth orbit in 2008.

INTRODUCTION

Improved spacecraft shield design requires early entry of radiation constraints into the design process to maximize performance and minimize costs. As a result, we have been investigating high-speed computational procedures to allow shield analysis starting with preliminary design concepts on to high fidelity final design models (Wilson et al. 2003). Of particular importance is the need to implement probabilistic models to account for design uncertainties (Wilson et al 2004a) in the context of optimal design processes (Qualls et al. 2003). In this report, we will discuss the progress towards a full three-dimensional and computationally efficient deterministic transport code for which the current HZETRN evaluates the lowest order asymptotic term in the context of a numerical marching procedure. Transport code verification was accomplished through convergence testing and benchmarking using restricted solutions with methods of characteristics (Wilson et al. 1988a) and also with Heaviside operational transform methods (Ganapol et al. 1991). The marching procedure is adequate for boundary conditions found in the space environment allowing space flight validation for nearly two decades using the Space Transportation System (STS) and the International Space Station (ISS) measured data. HZETRN is the first deterministic solution to the Boltzmann equation allowing field mapping within the ISS in tens of minutes using standard Finite Element Method (FEM) geometry common to engineering design practice (VerHage et al. 2002). This coupling enables development of integrated multidisciplinary design optimization methods.

In the present paper, we give the formalism for further developing a fully three-dimensional HZETRN code using marching procedures. In addition we describe the development of a new code based on Green's functions which is capable of not only validation in the space environment but also in the laboratory with directed beams of ions of specific energy and characterized with detailed diagnostic particle spectrometer devices (Tweed et al. 2005, Walker et al. 2005). A new version of the HZETRN code capable of simulating HZE ions with either laboratory or space boundary conditions for validation is under development. The computational model consists of combinations of physical perturbation expansions based on the scales of atomic interaction, multiple nuclear scattering, and nuclear reactive processes with use of asymptotic/Neumann expansions with non-perturbative corrections. This new code contains energy loss with straggling, nuclear attenuation, nuclear fragmentation with energy dispersion and downshifts. Off-axis dispersion with multiple scattering and light ion and neutron 3D propagation with full angular dependence are under preparation. A benchmark for a broad directed beam for 1 A GeV iron ion beams with 2 A MeV width and four targets composed of polyethylene, polymethyl metachrylate, aluminum, and lead of varying thickness from 5 to 30 g/cm² are also given. The benchmark quantities will be dose, track averaged linear energy transfer (LET), dose averaged LET, fraction of iron ion remaining, and fragment energy spectra after 23 g/cm² of polymethyl metachrylate. Flight and ground-based validation of the current codes and their associated database are discussed (Wilson et al. 2005a).

Our early interest in deterministic HZE transport code development paralleled the experimental studies of Walter Schimmerling et al. (1986) at the Lawrence Berkeley Laboratory that involved solving the Boltzmann transport equation for mono-energetic ion beams in the context of the continuous slowing down approximation and velocity conserving interactions (Wilson et al. 1984). The main computational limitation was found to be the inadequacy of available nuclear data ascertained by comparing computational results to the ionization data for a broad beam of ²⁰Ne ions (Wilson et al. 1984, Shavers et al. 1993). Emphasis was soon overtaken by the need to establish the scope of the galactic cosmic ray (GCR) protection problem, and marching procedures were used to get first order estimates of shielding requirements (Wilson et al. 1986, 1991). Validation of the new computational marching model against atmospheric air shower data again pointed to the inadequacy of the available nuclear data (Wilson and Badavi 1986) and development of a semi-empirical nuclear model followed, leading to reduced computational model errors (Wilson et al. 1987a, 1987b). HZETRN code verification was through numerical convergence and benchmarking with analytical solution (Wilson and Badavi 1986) and Heaviside methods (Ganapol et al. 1991). The next decade emphasized spaceflight validation (including human phantom testing) of the marching solution and nuclear model improvements (Shinn et al. 1998, Cucinotta et al. 1998, Wilson et al. 1995a, Badhwar et al. 1992, 1994, 2001, 2002). These codes were configuration controlled and accepted by OSHA and NASA STD-3000 (2005) for use in radiation safety and design.

Advanced solution methods of the Boltzmann equation continued to develop (Wilson et al. 1994a,b) but only slowly after NASA interest in deterministic transport code and nuclear model development waned in 1995 in favor of Monte Carlo methods (Armstrong and Colburn 2001, Pinsky et al. 2001) and their associated limitations (Wilson et al. 2002a). Recent renewed interest within NASA for deterministic code development to service the CEV design requirements is giving new emphasis to improved solution methods, but with no new nuclear modeling activity (Wilson et al. 2004b). As a result, current developments utilize the older semi-empirical NUCFRG2 model (Wilson et al. 1995a) with energy downshifts and momentum dispersion (Tripathi et al. 1994, Tweed et al. 2005). Comparison of NUCFRG2 nuclear fragmentation database with other models and iron ion beam experiments are given by Zeitlin et al. (1997) and Golovchenko et al (2002). In the current report, we will first review the current status of code development with emphasis on future needs. Only formal development will be given here, and the referenced material contains the details of the computational methods development. Within current limitations, we will present methods of code verification and recent spaceflight validation based on the marching procedures and laboratory validation using a newly developed code based on three-term Neumann expansions with nonperturbative corrections (Wilson et al. 1994a, 1994b) above the third Neumann term (Tweed et al. 2005).

DETERMINISTIC CODE DEVELOPMENT

The relevant transport equations are the linear Boltzmann equations derived on the basis of conservation principles (Wilson et al. 1991) for the flux density $\phi_j(\mathbf{x}, \boldsymbol{\Omega}, E)$ for particle type j as

$$\boldsymbol{\Omega} \cdot \nabla \phi_j(\mathbf{x}, \boldsymbol{\Omega}, E) = \sum_k \sigma_{jk}(\boldsymbol{\Omega}, \boldsymbol{\Omega}', E, E') \phi_k(\mathbf{x}, \boldsymbol{\Omega}', E') - \sigma_j(E) \phi_j(\mathbf{x}, \boldsymbol{\Omega}, E) \quad (1)$$

where $\sigma_j(E)$ and $\sigma_{jk}(\Omega, \Omega', E, E')$ are the shield media macroscopic cross sections. The $\sigma_{jk}(\Omega, \Omega', E, E')$ represent all those processes by which type k particles moving in direction Ω' with energy E' produce a type j particle in direction Ω with energy E (including decay processes). Note that there may be several reactions that produce a particular product, and the appropriate cross sections for equation (1) are the inclusive ones. Exclusive processes are functions of the particle fields and may be included once the particle fields are known. The total cross section $\sigma_j(E)$ with the medium for each particle type is

$$\sigma_j(E) = \sigma_{j,at}(E) + \sigma_{j,el}(E) + \sigma_{j,r}(E) \quad (2)$$

where the first term refers to collision with atomic electrons, the second term is for elastic scattering on the nucleus, and the third term describes nuclear reactions where we have ignored the minor nuclear inelastic processes (excited single particle states, except for low energy neutron collisions). The corresponding differential cross sections are similarly ordered. Many atomic collisions ($\sim 10^6$) occur in a centimeter of ordinary matter, whereas $\sim 10^3$ nuclear coulomb elastic collisions occur per centimeter, while nuclear reactive collisions are separated by a fraction to many centimeters depending on energy and particle type. We include in the $\sigma_{j,r}(E)$ term the nuclear decay processes.

Solution methods first use physical perturbations based on the ordering of the cross sections with the frequent atomic interactions as the first physical perturbation with special methods used for neutrons for which atomic cross sections are zero. The first physical perturbation to be treated is the highly directed atomic collisions with mean free paths on the order of micrometers as observed in nuclear emulsion. The usual approximation is the continuous slowing down approximation leading to well specified range-energy relations as shown in Fig. 1, but neglects the energy straggling that will be included in the present treatment. The next term is the highly directed multiple coulomb scattering and is usually neglected in many models but is of great importance in understanding the transport of unidirectional ion beams leading to beam divergence and so is treated in detail. The remaining nuclear reactive processes have been the main attention in past code developments. We will now consider the formal development of the relevant equations for further consideration.

We rewrite equation (1) in operator notation by defining a vector array of field function as

$$\Phi = [\phi_j(x, \Omega, E)] \quad (3)$$

the drift operator

$$D = [\Omega \cdot \nabla] \quad (4)$$

and the interaction operator

$$I = [\sum_j \sigma_{jk}(\Omega, \Omega', E, E') d\Omega' dE' - \sigma_j(E)] \quad (5)$$

with the understanding that I has three parts associated with atomic, elastic, and reactive processes as given in equation (2). Equation (1) is then rewritten as

$$[D - I_{at} - I_{el}] \bullet \Phi = I_r \bullet \Phi \quad (6)$$

where the first two physical perturbation terms are shown on the left-hand side and are represented by diagonal operators. The first order physical perturbation for atomic processes is the solution of

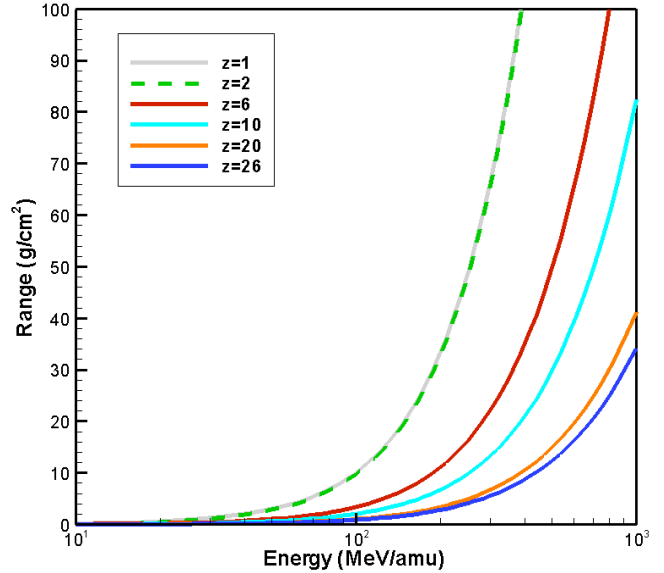


Fig. 1 Range of ions in aluminum.

The first physical perturbation to be treated is the highly directed atomic collisions with mean free paths on the order of micrometers as observed in nuclear emulsion. The usual approximation is the continuous slowing down approximation leading to well specified range-energy relations as shown in Fig. 1, but neglects the energy straggling that will be included in the present treatment. The next term is the highly directed multiple coulomb scattering and is usually neglected in many models but is of great importance in understanding the transport of unidirectional ion beams leading to beam divergence and so is treated in detail. The remaining nuclear reactive processes have been the main attention in past code developments. We will now consider the formal development of the relevant equations for further consideration.

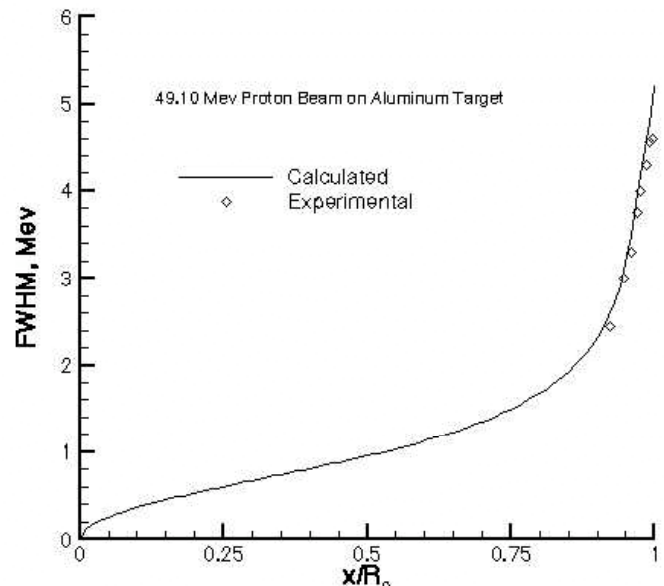


Fig. 2 FWHM of 49.1 MeV protons.

$$[D - I_{at}] \bullet \Phi = 0 \quad (7)$$

Using the moments methods is approximated by

$$\Phi(z, E) = \exp[-(E - \langle E(z) \rangle)^2 / (2s^2(z))] / (\sqrt{2\pi} s(z)) \quad (8)$$

where the array of mean residual energies $\langle E(z) \rangle$ is calculated from the range-energy relations given in Fig. 1 and the energy deviation due to straggling $s(z)$ are evaluated using a second order Green's function (Wilson et al. 2002b) and related to the full width at half maximum (FWHM) as shown in Fig. 2 for 49.1 MeV protons penetrating aluminum targets. As a result of energy straggling as given in equation (8), the unique relationship of penetration depth and particle energy as shown in Fig. 1 is no longer true. The fluence of penetrating protons in aluminum is represented by equation (8) and shown in Fig. 3 where the mean range is given by the curves in Fig. 1. Although the straggling correction for the uncollided beam with monoenergetic boundary functions is important, it is negligible in the higher order terms compared to the energy dispersion in nuclear reaction products.

The second physical perturbation term is the multiple coulomb scattering by the atomic nucleus as a solution of

$$[D - I_{ei}] \bullet \Phi = 0 \quad (9)$$

and represented by Rutherford scattering modified by screening of the nuclear charge by the orbital electrons using the Thomas-Fermi distribution for the approximation of atomic orbitals. We will utilize the multiple scattering solutions of Fermi given by

$$\Phi(z, r, \theta_r, \theta_t) = [\sqrt{3} w^2 / 2\pi z^2]^2 \times \exp[-w^2(\theta_t^2/z)] \times \exp[-w^2(\theta_r^2/z - 3r\theta_r/z^2 + 3r^2/z^3)] \quad (10)$$

where z is the longitudinal distance, r is the lateral distance, θ_r is the angle to the longitudinal axis in the r, z -plane, θ_t is the propagation angle perpendicular to the r, z -plane and w^2 the array of appropriate angular diffusion coefficients. Strictly speaking, the solution applies only over intervals for which the variation in ion energy is small. It follows that the mean square transverse angle (understood as a differential quantity) in traveling a distance dz is given from equation (10) as

$$\langle \theta_r^2 \rangle = 2 dz / w^2 \quad (11)$$

Conversely, one finds for a uniform nuclear charge distribution shielded by a Thomas-Fermi atomic structure

$$\langle \theta_r^2 \rangle = dz (Z_P E_s / \beta pc)^2 / X_0 \quad (12)$$

so that

$$w^2 = 2X_0 (\beta pc / Z_P E_s)^2 \quad (13)$$

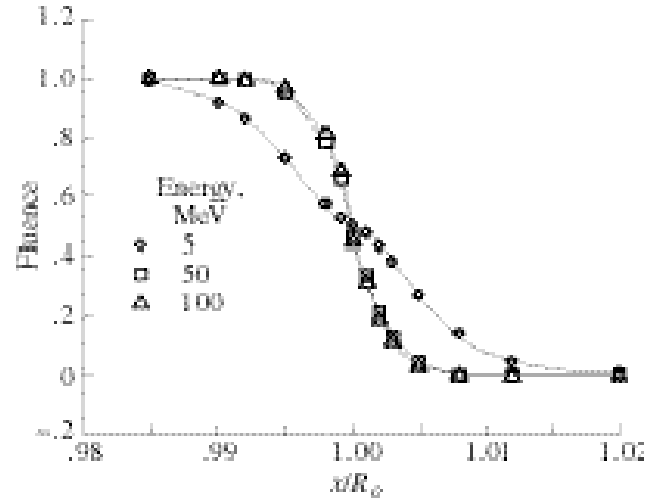


Fig. 3. Proton fluence near end of range in aluminum at three energies.

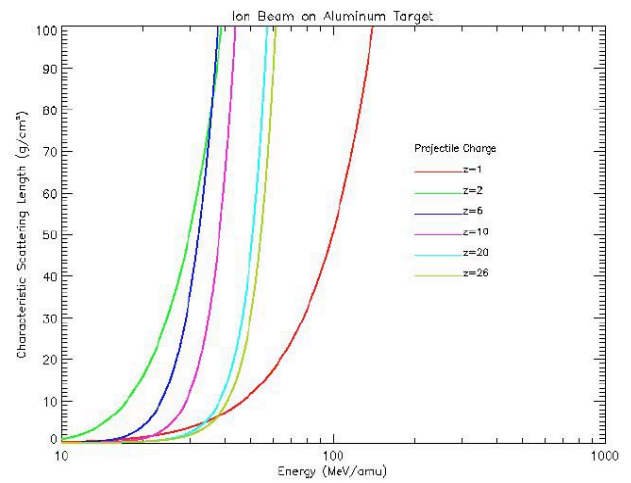


Fig. 4. Characteristic scattering length of various ions in aluminum.

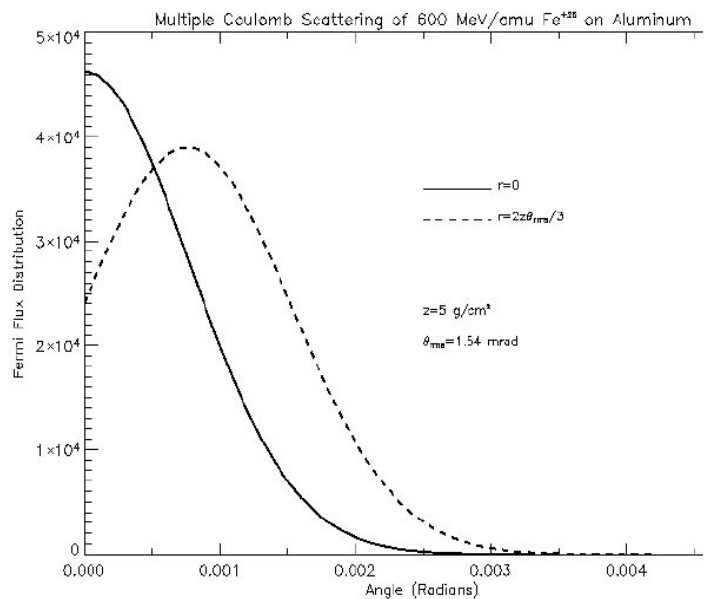


Fig. 5 Multiple Coulomb scattering of 600 A MeV iron ions in a 5 g/cm² aluminum target.

where

$$E_s = \sqrt{4\pi\mu_e^2/\alpha} = 21.2 \text{ MeV} \quad (14)$$

with α the fine structure constant, \mathbf{p} the ion momentum array, the array $\boldsymbol{\beta}$ of ion speeds relative to the speed of light c , \mathbf{Z}_p the array of projectile charges, and X_0 is the electron radiation length in the material (Fig. 4). The electron radiation length (g/cm^2) is given by

$$X_0^{-1} = 4\alpha (N_A/A) Z_T^2 r_0^2 \ln(181Z_T^{-1/3}) \quad (15)$$

with Avagadro's number N_A , A the molecular weight of the target material, and r_0 the classical electron radius. We will be using Schimmerling and coworkers modifications to Fermi's width formula (Schimmerling et al. 1986, Wong et al. 1989). The effects of energy variation on the variance in angle is given by

$$\langle \theta_r^2 \rangle = \int [(Z_p E_s / \beta p c)^2 / X_0] dE / S_j(E) \quad (16)$$

where the integral is over the energy range, and $S_j(E)$ is the stopping power. Multiple scattering played a critical role in prior experimental validation of the transport solutions (Shavers et al. 1990,1993). An example of multiple Coulomb scattering is given in Fig. 5 showing the emerging ion angular distribution on the beam axis and off the beam axis for 600 A MeV iron ions in aluminum. The iron ions on the beam axis remain highly peaked in the forward direction while those that have scattered off axis exhibit an angular divergence related to the longitudinal distance z and lateral distance r as $\theta_r = 3 r / (2 z)$. In all cases, the angular dispersion is small except at very large distances z and clearly will be mainly important only for the uncollided beam ions. To a first approximation, the off axis components are taken as directed along the central angle $\theta_r = 3 r / (2 z)$ with dispersion width of in-plane and out-of-plane given by equation (16) and treated in an asymptotic expansion about the central angle. Note that uncharged particles have no Coulomb scattering, and the main contribution to equation (9) is the nuclear elastic scattering and will be discussed later in the development.

The third order physical perturbation involves the relatively rare nuclear reactive processes represented by the operator I_r of equation (6). The probability of nuclear reaction in coming to rest is given in Fig. 6. It is seen from the figure helium ions have unit probability of nuclear collision above 500 A MeV and other ions will only reach unit probability of nuclear reaction above 1 A GeV. Although these nuclear processes are relatively rare, they represent large transfers of energy resulting in production of additional particles in the spacecraft interior environment which are at times more injurious than the particles of the space environment present at the boundaries of the spacecraft. The nuclear absorption term is a diagonal contribution and will be shifted to the left hand side with other purely diagonal terms while the integral contributions have both off-diagonal and on-diagonal parts and will remain on the right hand side as follows

$$[D - I_{at} - I_{el} + \sigma_r] \bullet \Phi = \{ \int \sigma_r(\boldsymbol{\Omega}, \boldsymbol{\Omega}', E, E') d\boldsymbol{\Omega}' dE' \} \bullet \Phi \equiv \bar{\Xi}_r \bullet \Phi \quad (17)$$

It is the control of secondary processes represented by the right hand side of equation (17) that is a controlling factor in reducing the radiation environment within a spacecraft. This is accomplished by choice of chemical composition of construction materials that must simultaneously meet other requirements of the service environment including loads, thermal, damage tolerance... (Wilson et al. 2002c, 2004a). The elements with off-diagonal nuclear reactive differential cross sections can be written in the following form

$$\sigma_{jk,r}(\boldsymbol{\Omega}, \boldsymbol{\Omega}', E, E') = \sigma_{jk,iso}(E, E') / 4\pi + \sigma_{jk,for}(\boldsymbol{\Omega}, \boldsymbol{\Omega}', E, E') \quad (18)$$

where the first term is isotropic and associated with lower energy particles produced including target fragments and the second term is highly peaked in the forward direction and is associated mainly with direct quasi-elastic events and projectile fragmentation products (Wilson 1977, Wilson et al. 1988a).

Surprisingly, even nucleon-induced reactions follow this simple form and the isotropic term extends to relatively high energies (see Fig. 7). For nucleon induced reactions, the following form has been used in early versions of FLUKA (Ranft 1980, Wilson et al. 1988b) as follows

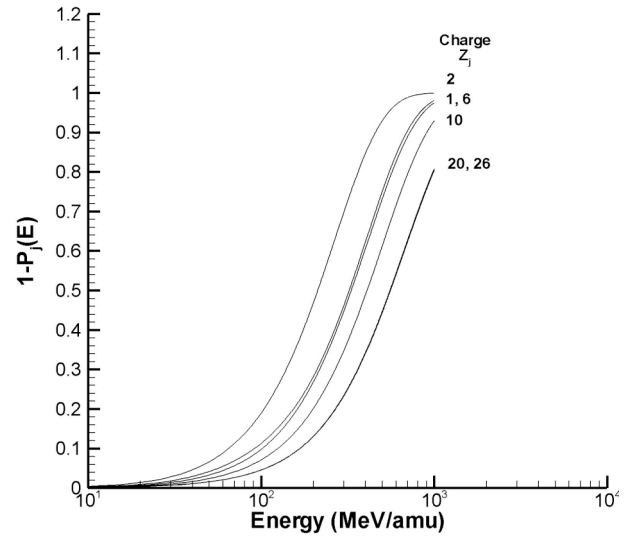


Fig. 6 Probability of nuclear reaction as a function of ion type and energy.

$$\sigma_{jk,r}(\Omega, \Omega', E, E') = v_{jk}(E') \sigma_{k,r}(E') f_{jk}(E, E') \times g_R(\Omega \bullet \Omega', E, A_T) \quad (19)$$

where $v_{jk}(E')$ is mean multiplicity and the Ranft factor used in FLUKA is

$$g_R(\Omega \bullet \Omega', E, A_T) = N_R \exp[-\theta^2/\lambda_R] \pi 2 \geq \theta \geq 0 \quad (20)$$

and constant for larger values of production angle θ , N_R is normalization constant, and λ_R given by Ranft as

$$\lambda_R = (0.12 + 0.00036 A_T/E) \quad (21)$$

although new generalized fits are being derived. This separation in phase space will be further exploited in computational procedures.

The heavy ion reaction cross sections have the general form (Wilson 1977) given by

$$\sigma_{jk,for}(\Omega, \Omega', E, E') = \sigma_{k,r}(E') [v_{jk}^P(E') f_{jk}^P(\Omega, \Omega', E, E') + v_{jk}^T(E') f_{jk}^T(\Omega, \Omega', E, E')] \quad (22)$$

where superscript P refers to projectile fragments and T to target fragments and are largely recognized by their separation in phase space. The heavy ion projectile fragment cross sections are further represented by

$$\sigma_{jk,for}^{\square}(\Omega, \Omega', E, E') = \sigma_{k,r}(E') v_{jk}^P(E') N_t \exp[-2m\sqrt{E'}(1-\Omega \bullet \Omega')/\epsilon_{t,jk}] \times \exp[-(E + \lambda_{jk} - E')^2/2 \epsilon_{jk}^2]/\sqrt{(2\pi\epsilon_{jk}^2)} \quad (23)$$

where λ_{jk} is related to the momentum downshift, ϵ_{jk} is related to the longitudinal momentum width, $\epsilon_{t,jk}$ is related to the transverse momentum width, and N_t is the transverse normalizing factor. Since the transverse width is small compared to the projectile and fragment energy the transverse function is highly peaked about the forward direction ($\Omega \bullet \Omega' \approx 1$). The nucleonic component spectral distribution in HZE collisions for quasi-elastic events is approximately given as

$$\sigma_{jk,for}^{\square}(\Omega, \Omega', E, E') = \sigma_{k,r}(E') v_{jk}^P(E') N_n \times \exp[-2m\sqrt{E'}(1-\Omega \bullet \Omega')/\epsilon_{t,jk}] \exp[-|E-E'|^R/2w_f^2] \quad (24)$$

where R is given in Shavers et al. (2001) as

$$R = 1.3108 + 0.883 \exp(-0.0038E') + 0.6933 \exp(-0.001E') \quad (25)$$

and the width w_f is given as

$$w_f = 197.3 \times (1.125 A_k)^{1/3} / \tau_k \quad (26)$$

where τ_k is the Fermi radius of the projectile ion k . Atomic interactions limit the contributions of charged particles in the transport process. For example, the protons and alpha particles produced in aluminum below 100 A MeV contribute to the fluence only within a few centimeters of their collision source and the heavier ions are even more restricted (see Fig. 1). This is an important factor in that the transported secondary charged particle flux tends to be small at low energies and the role of additional nuclear reactions are likewise limited (see Fig. 7).

The reaction cross section is separated by equation (18) into isotropic and forward component for which equation (17) may be written as coupled equations

$$[D - I_{at} - I_{el} + \sigma_r] \bullet \Phi_{for} = \{ \int \sigma_{r,for}(\Omega, \Omega', E, E') d\Omega' dE' \} \bullet \Phi_{for} \equiv \Xi_{r,for} \bullet \Phi_{for} \quad (27)$$

and

$$[D - I_{at} - I_{el} + \sigma_r] \bullet \Phi_{iso} = \{ \int \sigma_r(\Omega, \Omega', E, E') d\Omega' dE' \} \bullet \Phi_{iso} + \{ \int \sigma_{r,iso}(\Omega, \Omega', E, E') d\Omega' dE' \} \bullet \Phi_{for} \equiv \Xi_r \bullet \Phi_{iso} + \Xi_{r,iso} \bullet \Phi_{for} \quad (28)$$

Equation (27) is used to match the boundary conditions and can be written as a Volterra equation (Wilson 1977, Wilson et al. 1975, 1991, 1994a, 1994b) and solved as a Neumann series

$$\Phi_{for} = [G + G \bullet \Xi_{r,for} \bullet G + G \bullet \Xi_{r,for} \bullet G \bullet \Xi_{r,for} \bullet G + \dots] \bullet \Phi_B \quad (29)$$

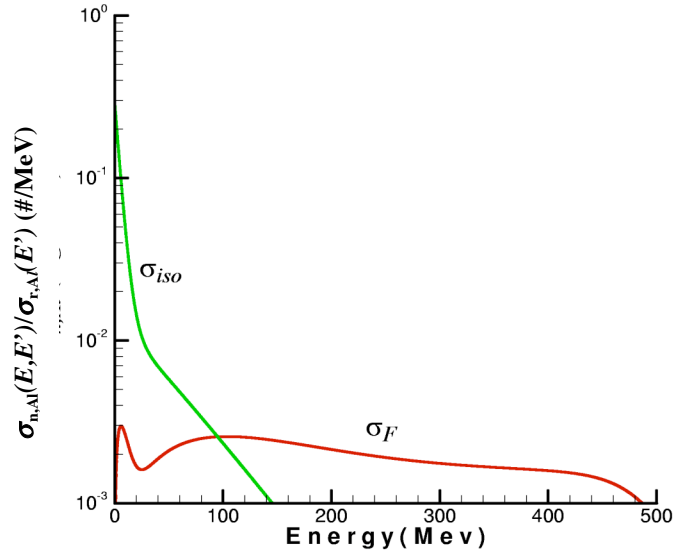


Fig. 7 Isotropic and forward neutron spectra produced by 500 MeV protons in aluminum.

for which the series can be evaluated directly as described elsewhere (Wilson et al. 1994a).

The cross term in equation (28) gives rise to an isotropic source of light ions of only modest energies and neutrons. The high-energy portion of the isotropic spectra arises from multiple scattering effects and the Fermi motion of the struck nucleons within the nucleus. The low-energy isotropic spectra arise from decay processes of the struck nucleus. Spectral contributions to the Neumann series depend on the particle range and probability of surviving nuclear reactions that establish the functional form of the \mathbf{G} matrix in equation (29). The second term of the Neumann series is proportional to the probability of nuclear reaction that is limited by the particle range as discussed above and shown in Fig. 6. It is clear from Fig. 6 that those nuclear reactions for the charged particles below a few hundred A MeV are infrequent providing fast convergence of the Neumann series (Wilson and Lamkin 1975). For the moment, we will neglect the straggling and multiple-elastic processes to simplify the present explanation (these provide only minor corrections to space radiation exposures but important in laboratory testing) and examine the remaining reactive terms of equation (27). The corresponding Volterra equation is given (Wilson 1977) by

$$\begin{aligned} \phi_j(\mathbf{x}, \boldsymbol{\Omega}, E) = \{S_j(E_\gamma)P_j(E_\gamma) \phi_j(\boldsymbol{\Gamma}(\boldsymbol{\Omega}, \mathbf{x}), \boldsymbol{\Omega}, E_\gamma) + \Sigma \int_E^{E_\gamma} dE' A_j P_j(E') \int_{E'}^\infty \int_{4\pi} dE'' d\boldsymbol{\Omega}' \sigma_{jk,for}(\boldsymbol{\Omega}, \boldsymbol{\Omega}', E', E'') \\ \times \phi_k(\mathbf{x} + [R_j(E) - R_j(E')] \boldsymbol{\Omega}, \boldsymbol{\Omega}', E'')\} / S_j(E) P_j(E) \end{aligned} \quad (30)$$

where $\boldsymbol{\Gamma}$ is the point on the boundary connected to \mathbf{x} along $-\boldsymbol{\Omega}$, $E_\gamma = R_j^{-1}[\rho - d + R_j]$, ρ is the projection of \mathbf{x} onto $\boldsymbol{\Omega}$, and d is the projection of $\boldsymbol{\Gamma}$ onto $\boldsymbol{\Omega}$. Equation (30) results from the first term of the Neumann series solution to equation (27). In the past we have expanded the angular integral over $\boldsymbol{\Omega}'$ asymptotically and implemented as a marching procedure (HZETRN, Wilson and Badavi 1986), as a perturbation expansion (Wilson et al. 1984), and by non-perturbative approximation (Wilson et al. 1994a) resulting in three distinct methods to evaluate the first order asymptotic terms, all of which have had extensive experimental validation (Shavers et al. 1993, Wilson et al. 1998, Shinn et al. 1998). Independent of the method used to evaluate the lowest order term, the first correction term is found by replacing the fluence in the integrand of equation (27) by the lowest order asymptotic solution as

$$\begin{aligned} \phi_j(\mathbf{x}, \boldsymbol{\Omega}, E) = \{S_j(E_\gamma)P_j(E_\gamma) \phi_j(\boldsymbol{\Gamma}(\boldsymbol{\Omega}, \mathbf{x}), \boldsymbol{\Omega}, E) + \Sigma \int_E^{E_\gamma} dE' A_j P_j(E') \int_{E'}^\infty \int_{4\pi} dE'' d\boldsymbol{\Omega}' \sigma_{jk,for}(\boldsymbol{\Omega}, \boldsymbol{\Omega}', E', E'') \\ \times \phi_{k,o}(\mathbf{x} + [R_j(E) - R_j(E')] \boldsymbol{\Omega}', \boldsymbol{\Omega}', E'')\} / S_j(E) P_j(E) \end{aligned} \quad (31)$$

where $\phi_j(\mathbf{x}, \boldsymbol{\Omega}, E)$ is found as an integral over the neighborhood of rays centered on $\boldsymbol{\Omega}$ using the lowest order asymptotic solution $\phi_{k,o}(\mathbf{x}, \boldsymbol{\Omega}', E'')$ along an adjacent ray directed along $\boldsymbol{\Omega}'$. Note that the boundary condition reached along $-\boldsymbol{\Omega}'$ enters through the lowest order asymptotic approximation and the angular integral correction in equation (30) is determined by the homogeneity and angular dependence of the space radiation and radius of curvature of the bounding material as we have shown long ago (Wilson and Khandelwal 1974, Wilson 1977). These are the determinant factors of the magnitude of the first order asymptotic correction that is anticipated to be very small for human rated systems (large radius of curvature) in space radiation that is homogeneous and isotropic in most applications (Wilson et al. 1991, Wilson et al. 1994b).

In a region of small radius of curvature the specific flux components near the site of evaluation will be missing contributions along adjacent rays that do not compensate losses along the ray on which the solution is evaluated representing the losses due to leakage. (Note, an asymptotic treatment of such small angle dependent phenomena is the only useful approach circumventing large discretization errors.) This computational procedure is only a small addition to prior code development and will have little impact on computational efficiency. The angular dependence of the integral kernel of equation (31) is controlled by the forward reactive cross section $\sigma_{jk,for}(\boldsymbol{\Omega}, \boldsymbol{\Omega}', E', E'')$ with its highly peaked structure given by equations (19, 23, 24) depending on particle type. The angular dependence of the forward peak of fragmenting Ca ions at 100 and 1,000

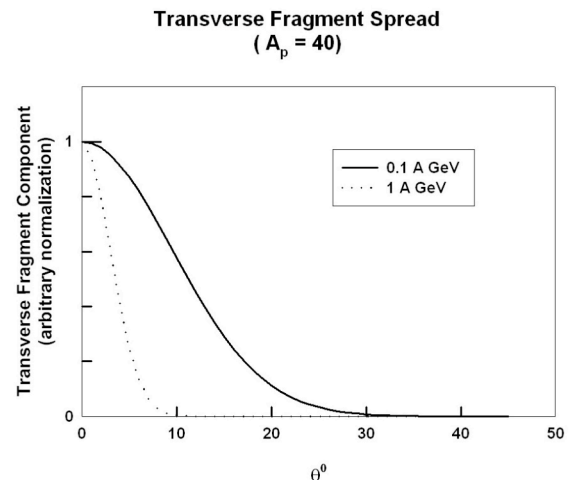


Fig. 8 Normalized transverse components for Ca fragmentation.

A MeV is shown in Fig. 8 as an example. The low-energy ions with limited range have transverse components on the order of 10 degrees reducing to a few degrees at high energies. It should be clear that the added divergence added by multiple Coulomb scattering of such fragments (Fig. 5) is negligible to the large angular widths of the fragmentation event (Fig. 8) further justifying equations (30 & 31).

Note that the low energy ions have limited range and will contribute little to the transported flux (see Fig. 1) or nuclear reactions (see Fig. 6). The higher energy ions, with their much longer pathlengths therefore giving more important added contributions to the particle fields, are related to only a very small angle of acceptance (few degrees) at the boundary. The form of the kernel leads directly to a Gauss-Hermite expansion and evaluation over the angle of production. Although the neutron Neumann series for the forward components converge more slowly since their contribution to the neutron flux is not limited by atomic interactions, these higher energy neutrons will be adequately evaluated by similar procedures. Higher order asymptotic terms can be evaluated with similar iteration of equation (31) if required but all indications are that the first such correction will be small for space radiation (Wilson and Lamkin 1975). This leaves the diffuse components of neutrons and light ions produced in the collision of the forward components and transported by equation (28) to be resolved (see for example, Cloudsley et al. 2000).

The transport from the low-energy neutron and light-ion isotropic sources in equation (28) dominates the solution below about 70 A MeV (see Fig. 7). In this region light-ion transport is completely dominated by the atomic interaction terms, and only a very small fraction have nuclear reactions making only minor additional contributions to the particle fields. This is especially true for the target fragments that can be solved in closed form (Wilson 1977, Cucinotta et al. 1990, 1991). The transport solution for the isotropic ion source terms to the lowest order perturbation is given by

$$\phi_{j,iso^o}(x,\Omega,E) = \Sigma \int_E^{E'} dE' A_j P_j(E') \int_{E'}^{\infty} \int_{4\pi} dE'' d\Omega' \sigma_{jk,iso,r}(\Omega,\Omega',E',E'') \phi_{k,for}(x+[R_j(E) - R_j(E')]\Omega,\Omega',E'') / S_j(E) P_j(E) \quad (32)$$

and will give highly accurate solutions to equation (28) since very few of the ions will have reactions (see Fig. 6), but could be easily corrected using the HZETRN light-ion propagator applied to the diffusive source terms. Note the E' integral effectively sums the ion source terms along direction Ω from the boundary to x . Also, the nuclear survival terms $P_j(E)$ are all near unity (see Fig. 6 showing $1 - P_j(E)$).

The neutrons have no charge and are undergoing, at low-energies, mainly elastic but also reactive nuclear processes. Although, equation (28) exhibits behavior similar to thermal diffusion, there are strong differences between thermal (heat conduction) and neutron diffusive processes. Thermal diffusion at ordinary temperatures has minor leakage through near boundaries since radiative processes are proportional to fourth power of temperature (in the absence of convection) leaving lateral diffusion across the media an important process. In distinction, neutron diffusion is dominated by leakage at near forward and backward boundaries and lateral diffusion plays a minor role. Generally, low-energy neutron leakage is a dominant process within 15-20 g/cm² of the bounding surface in most materials. Since human rated systems have shields of large radius of curvature and small thickness to radius ratio as determined by living and working space requirements, it approximates a connected system of flat plates for which leakage at forward and backward boundaries dominates the neutron transport. In this limit, neutron transport simplifies to a sequence of approximate 1D-transport problems with leakage at the back and forward boundaries and shows reasonable success in comparison with experimental flight data (Cloudsley et al. 2000, 2002). In the present development we will consider a convergent series of approximations to gauge accuracy of the transport procedures and allow choices of the most practical method.

The first term for diffusive neutron transport uses the lowest order perturbation similar to equation (32) given as

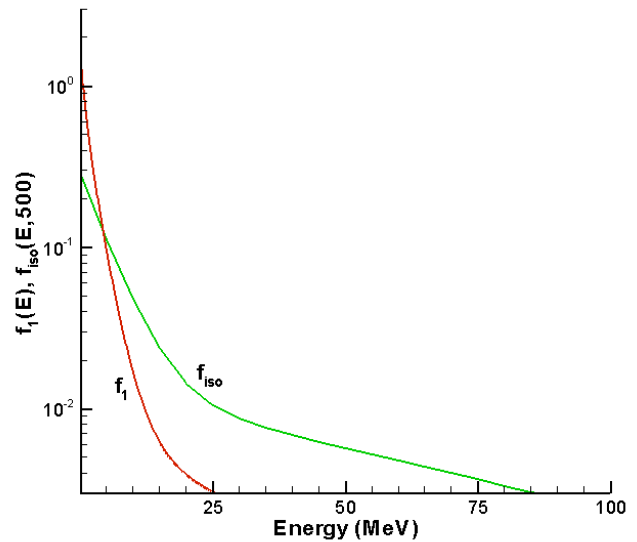


Fig. 9 Spectral dependence of diffuse isotropic neutron source term (eq. 33) and the first collision source term (eq. 34).

$$\phi_{n,iso}^o(x,\Omega,E) = \Sigma \int_0^{\rho-d} dx' \exp[-\sigma_n(E)x'] \int_{E'}^{\infty} \int_{4\pi} dE'' d\Omega' \sigma_{jkisor}(\Omega,\Omega',E',E'') \phi_{k,for}(x-x',\Omega,\Omega',E'') \quad (33)$$

where $\rho-d$ is the distance along $-\Omega$ from x to the boundary, x' is the distance from x to the source point along $-\Omega$, and $\sigma_n(E)$ is the total neutron cross section (elastic plus nonelastic). Note that equations (32) and (33) transport all particles (charged and uncharged) associated with the collisions of the forward component Φ_{for} found as solution to equation (27). The second collision term associated with the diffuse charged particle field given by equation (32) is negligible, but additional source terms from the lowest-order diffuse neutron solution given by equation (33) provides a strong source of diffuse neutrons. The added transport of these neutrons is given by

$$[\mu\Omega \cdot \nabla + \sigma_n(E)]\phi_{n,iso}^l(x,\Omega,E) = \int \sigma_n(\Omega,\Omega',E,E')d\Omega'dE'\phi_{n,iso}^l(x,\Omega',E') + \int \sigma_{nr}(\Omega,\Omega',E,E')d\Omega'dE'\phi_{n,iso}^o(x,\Omega',E') \quad (34)$$

where $\phi_{n,iso}^l(x,\Omega,E)$ is the remaining diffuse neutron component. The source term to the far right of equation (34) have been solved in exact 3D geometry, and the energy spectrum is much degraded from the source term in equation (33). Typical spectra of the sources in equations (33) and (34) are shown in Fig. 9. It is clear from the properties of the second collision source term that the diffuse spectra of neutrons from this term are highly degraded in energy and the methods developed in the nuclear engineering community for reactor applications are fully applicable, and our final attention turns to solution of equation (34). Note that the software prepared for equation (34) is also applicable to nuclear reactor shielding issues with appropriate source terms.

The dominant contribution to the low-energy neutron transport in most materials is elastic scattering from the media nuclei. In our shell FEM geometry, equation (34) can be written as

$$[\mu\partial_x + \sigma_n(E)]\phi_{n,iso}^l(x,\mu,E) = \int \sigma_n(\Omega,\Omega',E,E')d\Omega'dE'\phi_{n,iso}^l(x,\mu',E') + \int \sigma_{nr}(\Omega,\Omega',E,E')d\Omega'dE'\phi_{n,iso}^o(x,\Omega',E') \quad (35)$$

where $\mu = \Omega \cdot \mathbf{e}_x$, $\mu' = \Omega' \cdot \mathbf{e}_x$, the last term on the right is the source term from the forward scattered particle collisions. The elastic scattering term in equation (35) has a unique angular contribution $\mu_0 = \Omega \cdot \Omega'$ for a given energy transfer ($E' - E$) relating to a unique direction μ' under the integral. Standard spherical harmonic expansions of the cross sections and flux are made to develop a solution. As example, first order Legendre expansion (P1 approximation) gives the forward and backward flux as

$$\phi_{F,B} = 0.5 \phi_0 \pm 0.75 \phi_1 \quad (36)$$

where ϕ_0, ϕ_1 are the Legendre coefficients of $\phi_{n,iso}^l(x,\mu,E)$ with approximate transport equation given as we have used in the past (Cloudsley et al. 2000) using multigroup and collocation methods.

The multigroup transport of the diffuse neutrons in multilayered flat plate geometry with variable front and back boundaries in which the ions are treated in the lowest order asymptotic approximation is the current production code HZETRN. The first improvement would be to treat the diffuse ion components with perturbations from the neutron diffuse component giving a complete flat plate code in lowest asymptotic order with multigroup neutrons and diffuse ion components. To this, we will add the first asymptotic correction. This will provide NASA with an interim HZETRN production code for engineering design process development. In addition to the above, we will add mesons and electromagnetic cascades in the near future (Blattnig et al. 2004, 2005, Nealy et al. 2002, Anderson et al. 2004). At each step of future improvements, the corresponding codes will be integrated into the Space Ionizing Radiation Environments and Shielding Tools on the Framework for Analysis and Collaborative Engineering (SIREST/FACE) environment (Singleterry et al. 2001) with environmental models for NASA use (the current production code resides there already).

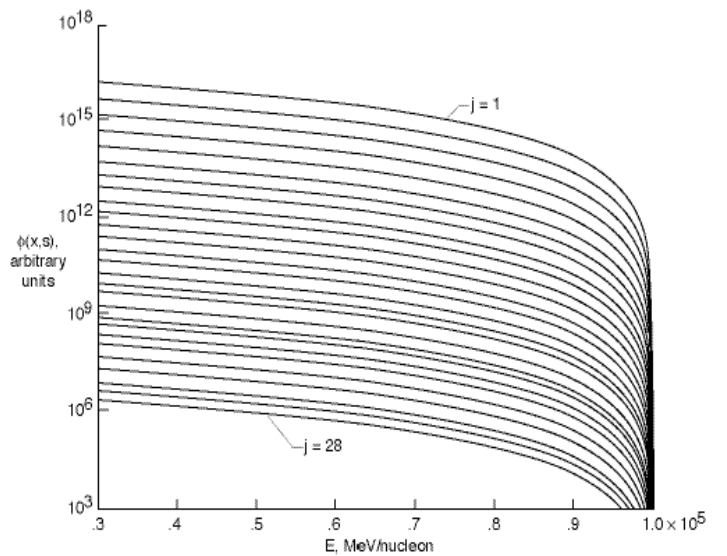


Fig. 10. Fluence profile with marching procedures that are indistinguishable from the Heaviside solutions of Ganapol et al (1991).

VERIFICATION

The solution using marching procedures is dependent on step size and energy grid, and convergence to 1 percent in the first 200 g/cm² of material is typically used for shield effectiveness evaluation (Wilson et al. 1991). The solution also depends on the isotopes represented in the calculation. Early versions of the code represented only the spectrum of 28 charges (H through Ni) plus neutrons. In this case, the fluence of hydrogen ions was the sum of proton, deuteron, and triton fluence combined and left the individual isotopes undefined. The marching procedures of this code was benchmarked against a Heaviside solution with a simplified stopping power and fragmentation parameter set allowing such techniques (Ganapol et al. 1991). The comparison of the marching solution and the Heaviside solution is indistinguishable as shown in Fig 10 demonstrating the high accuracy of the HZETRN algorithm.

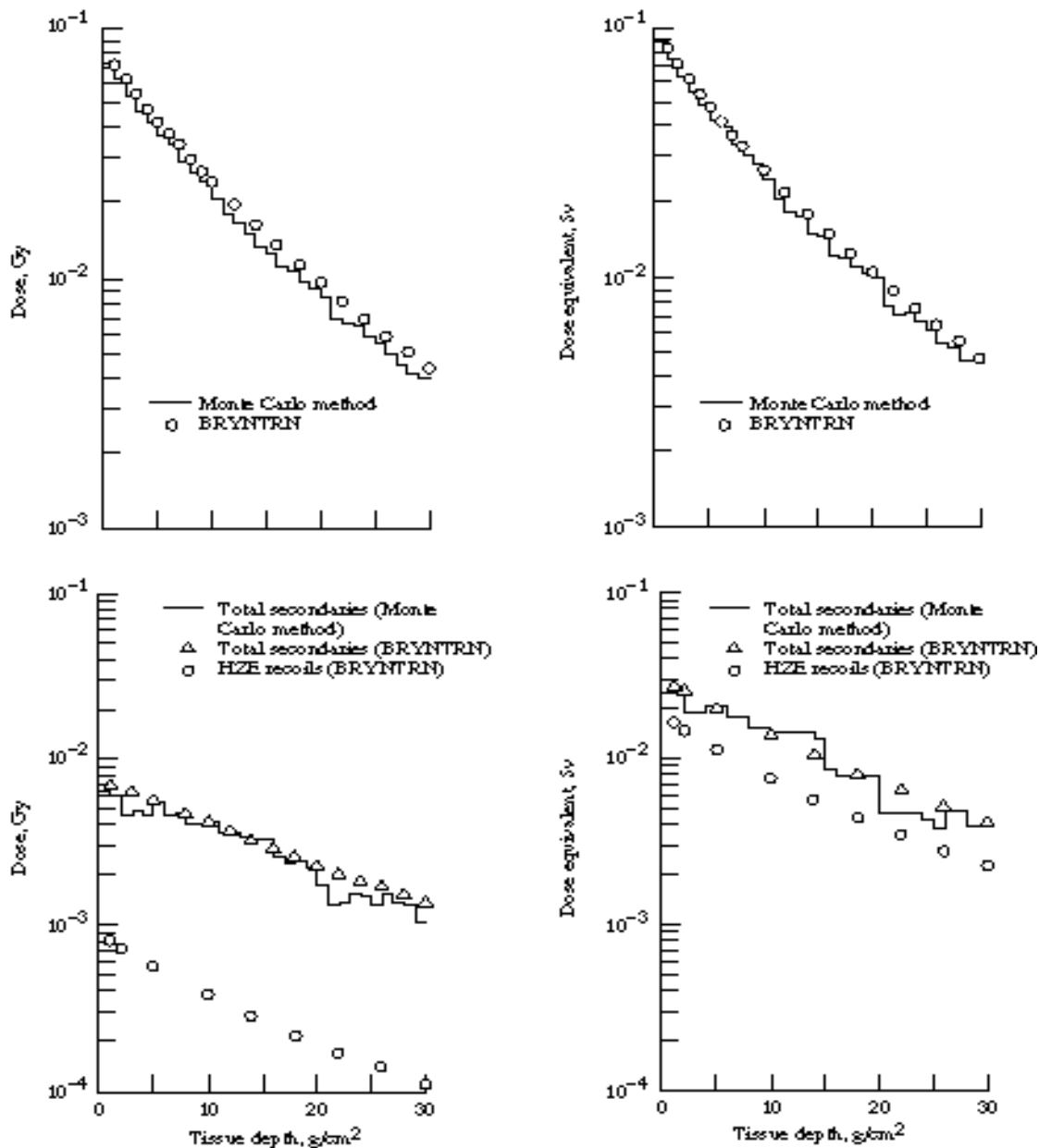


Fig. 11. Dose (left panels) and dose equivalent (right panels) for a rigidity spectrum with rigidity parameter of 100 MV incident on 20 g/cm² iron shield ahead of 30 cm tissue. Penetrating primary contributions (top panels) and secondary contributions (lower panels).

Monte Carlo methods were the first to develop under the Apollo program for spacecraft design. The High Energy Transport Code (HETC) developed at Oak Ridge National Laboratory for space use under NASA contract had at its core the Bertini intranuclear cascade model with a strong experimental validation effort and the low energy neutron data files of the nuclear energy program (Bertini et al. 1972, Alsmiller 1967). Although an accurate procedure, the computational burden even in simple geometry limited their usefulness in practical applications. Simpler and less accurate computational models were finally used in Apollo design and operations as the computational burden made HETC impractical. Only in the Shuttle operations era were improved computational procedures developed allowing computational efficiency based on the marching procedures discussed herein (Wilson et al. 1988c, 1991). The HETC code in simple geometry allowed verification of these new computational procedures and database were reasonably correct. One such comparison consisted of the benchmark using a solar particle event rigidity spectra based with rigidity parameter of 100 MV. The comparison of the marching procedure with the HETC computation for a 20 g/cm² iron shield of 30 cm of tissue is shown in Fig. 11. It is clear that the marching procedures and preliminary database give a fair representation of such integral quantities as dose and dose equivalent for typical solar particle events.

A benchmark for analytic solution again confirmed convergence to better than 1 percent (Wilson et al. 1988a). A convergence test by adding isotopes representing masses from 1 to 58 with neutrons indicated convergence to 1 percent in dose equivalent for the full galactic cosmic ray spectrum and was the standard used until recently. Isotope representation for particle fluence measurements for iron beams required a 122 isotope representation (Kim et al. 1994). Recently the galactic cosmic ray isotope distribution was increased to 170 isotopes and the corresponding isotope distribution in the transport model includes all such isotopes with expected convergence in dose equivalent to be much less than 1 percent (Cucinotta et al. 2003). Many more years of experience has been gained in validation with both ion beams and in spaceflight. By far the most important validation of the transport codes has been the laboratory validation process where both atomic and nuclear interaction details of movement through the material are gained. But

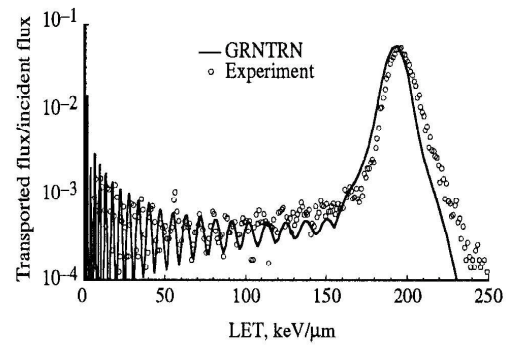


Fig. 12. Let spectra of a 557 A MeV iron beam measured in nuclear emulsion in a layered shield arrangement of 2.24 g/cm² of lead followed by 2 g/cm² aluminum (Shinn et al. 1994).

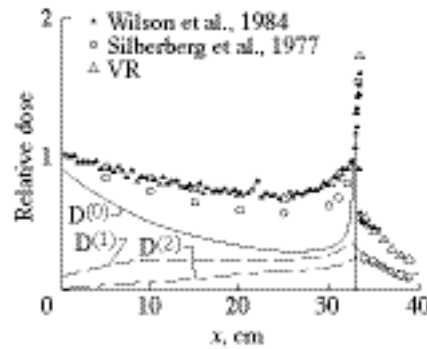


Fig. 13. Energy deposition in water by ²⁰Ne ions at 670 A MeV as evaluated using Green's functions and the Silberberg et al. (1977) nuclear model and the VR correct model.

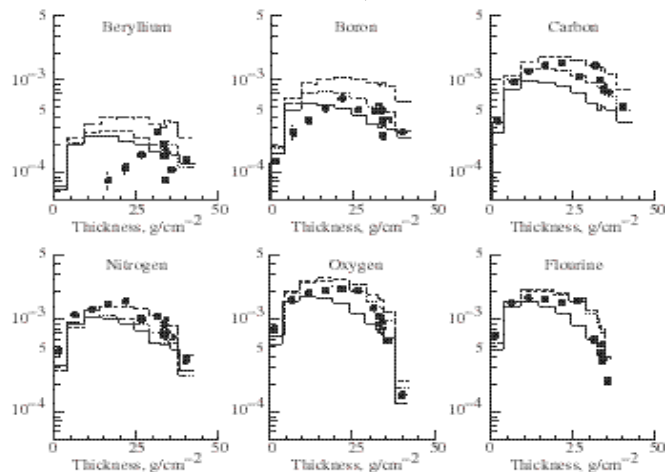


Fig. 14. Integral fluence of fragments produced by 636 A MeV neon ions in water of varying thickness.

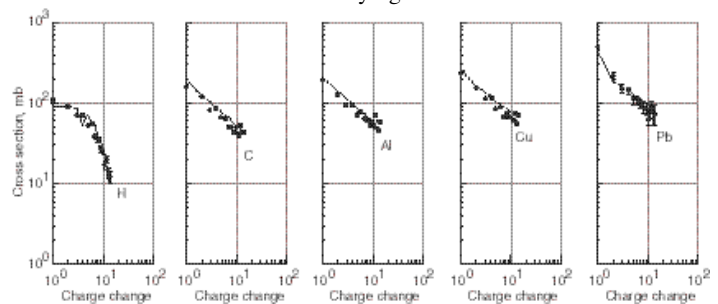


Fig. 15. Charge-changing cross sections for ΔZ from -1 to -14 for 1.05 GeV/nucleon ⁵⁶Fe incident on H, C, Al, Cu, and Pb targets. The solid lines are predictions from NUCFRG2 database generator.

spaceflight validation has the overall ability to test adequacy of shield modeling tools, environmental models, and transport models. Such a complex test has the disadvantage of ambiguity of errors that can enter the validation in different ways. To test environmental model errors, we have relied more on the better defined shielding model of the Shuttle in which high resolution measurements have been made over long periods of time.

ION BEAM VALIDATION

The current status of computational procedures are detailed by Tweed et al. (2005) with validation of these procedures by Walker et al. (2005). In the past we have found most useful the direct comparison of energy loss spectra either measured in nuclear track detectors (Shinn et al. 1994, Golovchenko 2002) or in silicon detectors (Wilson et al. 1984, Shavers et al. 1993, Wilson et al. 1998). An example of validation using nuclear track detectors is shown in Fig. 12. In this case, the target consists of two layers of materials, lead is the first target encountered by the beam and is followed by an aluminum target. The peak on the far right is the penetrating iron ions that have either survived penetrating the target or have only neutrons removed in interactions. The widths of the peaks are mainly a result of the resolution of the detectors and not a characteristic of the ion beam or interactions with the target. Validation with electronic detectors began with the laboratory tests of neon ion beams by Schimmerling and coworkers using a water column and ion chambers shown in Fig. 13. Also shown in the figure are model results of Wilson et al. (1984) in which the nuclear model used was a critical issue and replacement of the “state-of-the-art model” developed by the Naval Research Laboratory (Silberburg et al. 1977) required correction and finally replacement with software using a new nuclear model named NUCFRG (Wilson et al. 1987a, 1987b). The curves $D^{(0)}$, $D^{(1)}$, and $D^{(2)}$ are successive perturbation terms using the Wilson et al (1984) corrected cross sections. A further comparison of the fragment fluence is shown in Fig. 14. Note detector efficiency problems for the Be and B fragments (Shavers et al. 1993). Blind cross section testing by Zeitlin et al. (1988) confirms the usefulness of the NUCFRG model (Fig. 15).

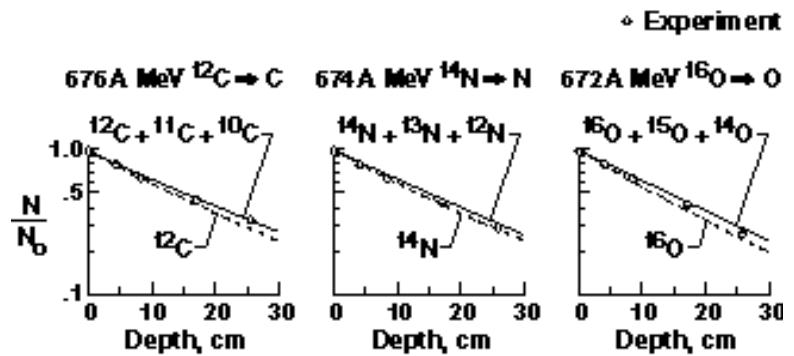


Fig. 16. Attenuation of primary beam particles (dash) and secondaries formed by neutron removal (solid).

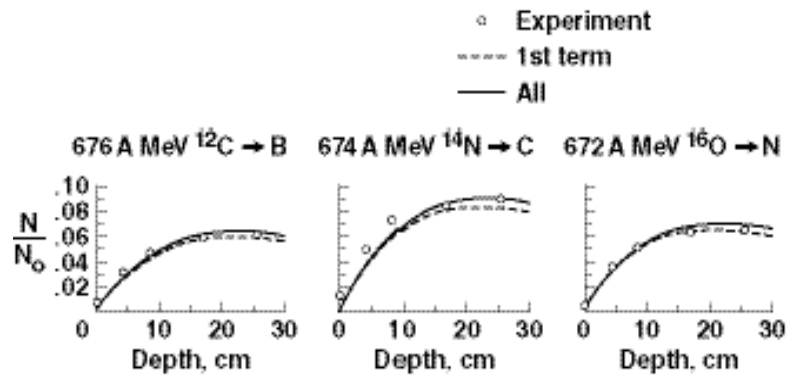


Fig. 17. Secondaries produced by removal of one proton.

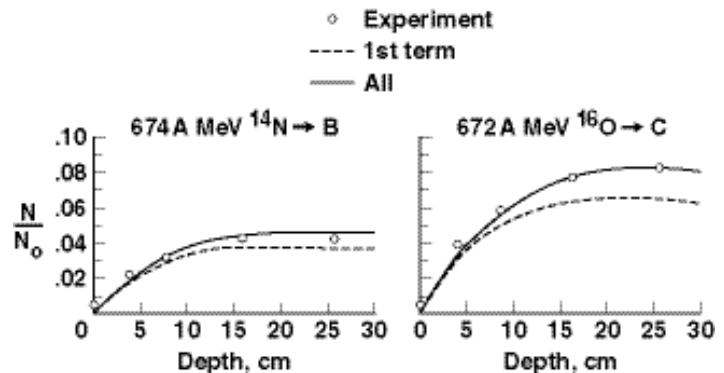


Fig. 18. Secondaries produced by removal of two protons including alpha clusters.

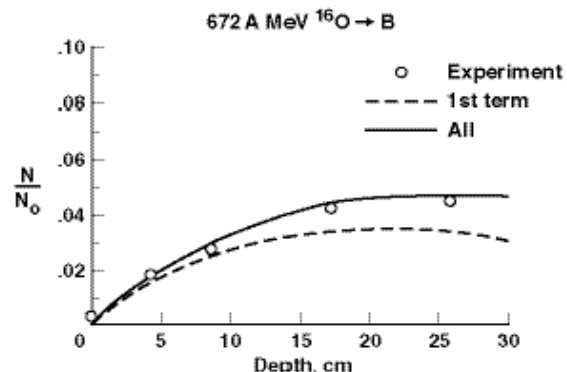


Fig. 19. Secondaries produced by removal of three protons.

Further laboratory testing of LET spectra at several depths in water using electronic detectors (Shavers et al. 1993) showed reasonable agreement with the Langley nuclear, atomic and transport models.

Experiments were performed at the Gesellschaft für Schwerionenforschung (GSI) accelerator using beams of ^{12}C , ^{14}N , and ^{16}O at energies of $674(\pm 2)\text{A MeV}$ in which the transmitted flux of charge 5 to 8 were measured behind a water target of variable thickness (Schall, 1994; Schardt *et al.*, 1995; Sihver *et al.*, 1995). The measured transmitted fluence of all ions of the same charge as the beam (open circles) is shown in Fig. 16 along with the solution for the primary beam fluence (dashed curve) and the calculated fluence of all ions of charge equal to the initial beam (solid curve). It appears that the total absorption and neutron removal cross sections of the NUCFRG2 are reasonably correct (see also Golovchenko et al. 2002). The measured fluence of all ions with a single charge removed (open circles) is shown in Fig. 17. The NUCFRG2 code including alpha knockout processes shown as the first collision term (dashed) and the complete solution (solid) is in reasonable agreement with the experiments. The measured fluence for removal of two charge units from the initial beams of ^{14}N and ^{16}O (open circles) is shown in Fig. 18 with the NUCFRG2 results. The effects of alpha clustering is most apparent in the alpha knockout process for ^{16}O collisions (Figure 18, right panel). The carbon isotope distribution in highly nonelastic collisions are equally distributed between ^{12}C and ^{13}C as can be seen in ^{40}Ar fragmentation (Tull, 1990). In distinction, the fragmentation of ^{16}O shows the single alpha knockout cross section to cause an excess of ^{12}C fragments being produced (Olson *et al.*, 1983, Cucinotta and Dubey 1994, Wilson et al. 1998). The addition of the alpha knockout cross section leaving the ^{12}C core in the ground state to the NUCFRG2 nonelastic cross section (solid curve) brings good agreement with the GSI oxygen beam data. The carbon fragments produced on the first collision is discussed by Wilson et al. (1998). The only triple charge removal data is for the ^{16}O ion beam as shown in Fig. 19 for which the NUCFRG2 is in reasonable agreement.

High resolution electronic detectors have the added advantage of allowing the detailed testing of the nuclear and atomic interaction database as well as the computational models. The detector arrangement is shown in Fig. 20. The detectors upstream from the target are used to identify the incoming ion to insure it is in fact a beam particle and not a fragment produced along the beam pipe. Following the target are additional analyzing detectors to characterize the particles leaving the target. The detector responses are determined by the solution of equation (1) and are closely related to the straggling solutions in equation (8). Although multiple scattering was prominent in the older setup, such effects

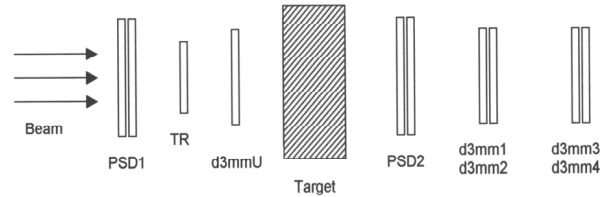


Fig. 20. Detector configuration (not to scale). All detectors are silicon; the trigger detector TR detector effectively defines the size of the usable beam spot. The respective thicknesses and approximate active areas are: TR – $300\ \mu\text{m} \times 300\ \text{mm}^2$; PSD1 and PSD2 – $1\ \text{mm} \times 1500\ \text{mm}^2$; d3mmU and d3mm1-4 – $3\ \text{mm} \times 450\ \text{mm}^2$.

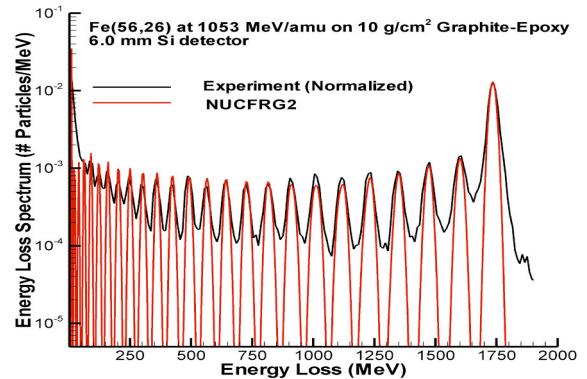


Fig. 21. Summed energy loss (MeV) in the detector pair d3mm3 and d3mm4 for fragments produced by $1037\ \text{A MeV } ^{56}\text{Fe}$ ions in $10\ \text{g/cm}^2$ graphite-epoxy (50.92/49.08%).

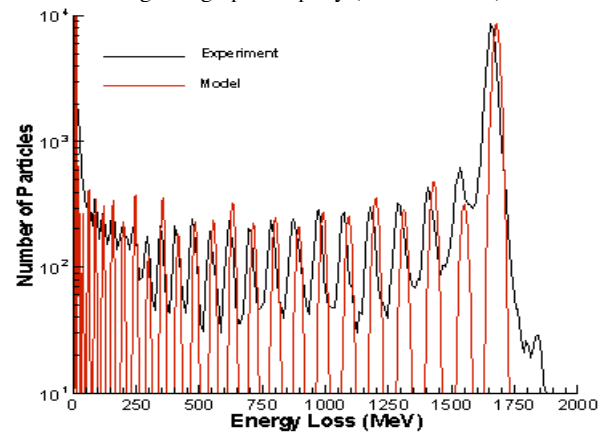


Fig. 22. Summed energy loss (MeV) in the detector pair d3mm3 and d3mm4 for fragments produced by $1037\ \text{A MeV } ^{56}\text{Fe}$ ions in $5\ \text{g/cm}^2$ graphite-epoxy (50.92/49.08%).

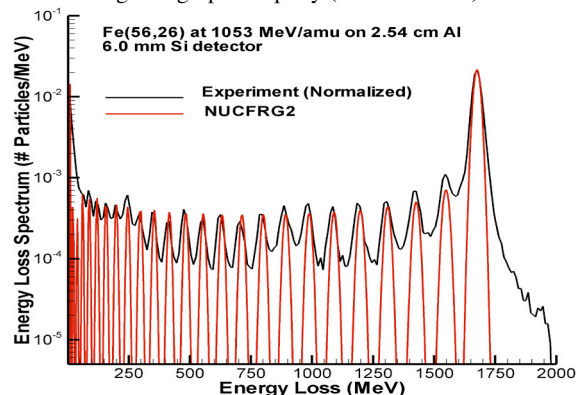


Fig. 23. Summed energy loss (MeV) in the detector pair d3mm3 and d3mm4 for fragments produced by $1037\ \text{A MeV } ^{56}\text{Fe}$ ions in $2.54\ \text{cm Al}$.

are minimized in the present apparatus. In modeling the experiment described above, it was assumed that the ^{56}Fe beam extracted from the AGS at 1037 A MeV was nearly monoenergetic (the small inherent energy width had no influence on subsequent comparisons as the main width comes from the detectors and the target). The Green's function solution (Tweed et al. 2005) was used to estimate the flux of the fragments entering the detector pair d3mm3 and d3mm4, which were treated as a single 6mm detector. The energy deposited by each fragment was then computed by means of equations (8) and used to evaluate the energy loss spectrum using the NUCFRG2 nuclear database (Wilson et al 1987b). The results (Tweed et al. 2003, Walker et al. 2005) are exhibited in Figs. 21 through 23 where the computed energy loss spectrum (red curve) is compared with the experimental measurements (black curve).

The right hand peak is from the surviving ion beam and fragments produced by neutron removal. The area associated with this peak is determined by the nuclear absorptive and neutron removal cross sections. The peak location and width are determined mainly by the range-energy relations and straggling process respectively. Clearly the comparison of the right most peak to the model is a strong test on these limited processes. The next peak to the left is for Mn fragments followed by Cr fragments and so on. These successive peaks are mainly governed by the fragmentation process and the area relates to the fragmentation cross section while the location and width is mainly determined by the energy down shift and energy dispersion on fragmentation. Hence the most accurate evaluation of the computational model lies in such comparisons. It appears that the Mn fragments are under-represented by the NUCFRG2 model for graphite/epoxy targets, which is consistent with earlier cross section measurements (Zeitlin et al. 1997). Overall, the fragmentation cross sections in Al seem better represented by NUCFRG2 than those for the graphite-epoxy composite. More recent results from the Quantum Multiple Scattering Fragmentation (QMSFRG) model may give some improvements (Cucinotta et al. 2003) over results in Figs. 21-23. An additional discrepancy is the energy downshift parameter for large mass removal especially for vanadium and lighter fragments. A further limitation of the model is for the lightest fragments (especially hydrogen and helium) that are produced with a broad spectrum resulting in a broad range of energy losses on the left margin of the measurements. This broad spectrum will be treated in later model development. The next emphasis will be on effects of multiple scattering and off-axis production components of ion fragmentation. Such effects will give improvements in the valley regions of the modeled results shown in Figs. 21 through 23.

In order to further validate the model, it is desirable to compare with more than just the energy deposited in the detectors but to compare integrated quantities used in radiobiology to express the character of the beam. It is advantageous to make comparisons of the computational model with data that is derived from the fluences emerging from the target. The easiest and perhaps most important of these integrated quantities to compare with is the track average LET, $\langle \text{LET} \rangle_{\text{trk}}$. The $\langle \text{LET} \rangle_{\text{trk}}$ can be computed from the formula

$$\langle \text{LET} \rangle_{\text{trk}} = \frac{\sum_j \int d\Omega \, dE \, L_j(E) \, \phi_j(\mathbf{x}, \Omega, E)}{\sum_j \int d\Omega \, dE \, \phi_j(\mathbf{x}, \Omega, E)} \quad (37)$$

where $\phi_j(\mathbf{x}, \Omega, E)$ is the flux and $L_j(E)$ is the LET of the j particle type at energy E . In order to be able to make comparisons with experimental data, we will take $S_j(E)$ to be that in water for particle j at energy E ; i.e., the stopping power for water.

The light ions, $Z_j = 1, 2$ have a strong angular dependence and, as a consequence of the straightahead approximation currently used in the model, there is a marked over prediction in their fluences. If uncorrected, the predictions for the $\langle \text{LET} \rangle_{\text{trk}}$ would be drastically lower than experiments, due to the artificial inflation of the denominator in equation (37). It is possible to correct for this by scaling $Z_j = 1, 2$ by an appropriate weight factor for each of the light ions, thereby reducing their number and dampening the effect. The weight factors are 0.02 for $Z_j = 1$ and 0.08 for $Z_j = 2$. These corrections are used for all targets and ^{56}Fe beams (Walker et al. 2005). Our ability to improve on these estimates will be limited by the lack of a supporting nuclear physics program with improvements as time available basis.

Table 1 shows $\langle \text{LET} \rangle_{\text{trk}}$ computed from the model with the corrected fluences and preliminary results from experiments done at Brookhaven National Laboratory Alternating Gradient Synchrotron (BNL AGS) for various targets and thickness. All of the experiments were carried out with a 1 A GeV ^{56}Fe beam. In all cases, there is

Table 1: Track Averaged LET from Model and Experiments. Angular factor for $z=1$ (2) is 0.02 (0.08)

Material	Depth (g/cm ²)	$\langle \text{LET} \rangle_{\text{trk}}$ model*	$\langle \text{LET} \rangle_{\text{trk}}$ experiments
Carbon	3.9	125.3	127.0
Aluminum	7	127.3	125.4
Lead	3.6	148.2	145.8
Polyethylene	10	91.3	91.4
Graphite-Epoxy	5	116.3	121.3
Graphite-Epoxy	10	94.8	98.5

reasonable agreement between the predictions of the model (± 5 percent) and the experimental results with the greatest error occurring in the results for graphite-epoxy.

Despite the clear advantage of direct comparison to detector output and its relation to atomic and nuclear processes, it has been the decision of the NASA Space Radiation Shielding Program to work with reduced quantities such as those given in Table 1. Recently, a benchmark was defined by 1 A GeV ^{56}Fe ion beams in polyethylene, polymethyl metachrylate (PMMA), aluminum, and lead at several depths. The benchmark quantities requested are for shielding materials program are:

Dose (unit ^{56}Fe fluence):

$$D(x) = K \sum_j \int d\Omega dE L_j(E) \phi_j(x, \Omega, E)$$

Track averaged LET:

$$\langle \text{LET} \rangle_{\text{trk}} = \frac{\sum_j \int d\Omega dE L_j(E) \phi_j(x, \Omega, E)}{\sum_j \int d\Omega dE \phi_j(x, \Omega, E)}$$

Dose averaged LET:

$$\langle \text{LET} \rangle_{\text{dose}} = \frac{\sum_j \int d\Omega dE L_j(E)^2 \phi_j(x, \Omega, E)}{\sum_j \int d\Omega dE L_j(E) \phi_j(x, \Omega, E)}$$

Fraction of Fe-ions:

$$F_{\text{surviving}}(x) = \frac{\int d\Omega dE \phi_j(x, \Omega, E)}{\text{incident ion fluence (unity)}}$$

For the targets of polyethylene, polymethyl metachrylate (PMMA), aluminum, and lead over the thickness range of 5 to 30 g/cm². In addition to the quantities requested, fragment spectra in PMMA as

Fragment spectrum at 23 g/cm² PMMA:

$$F_j(x, E) = \frac{\int d\Omega \phi_j(x, \Omega, E)}{\text{incident ion fluence (unity)}}$$

where K is conversion from MeV/g to nGy (K=1.602). In that the full angular dependence is lacking in the present computational model (Tweed et al. 2005), we have fit a renormalization constant to the light ion data of Zeitlin, Miller, and Heilbronn with resulting values of 0.02 (Z=1) and 0.08 (Z=2) as discussed by Walker et al. (2005). The dose, track and dose averaged LET, and fraction of surviving Fe-ions are given in Table 2. The iron ion range, R₀, for each target material is given in the table. The fragment spectra penetrating 23 g/cm² of PMMA are given in Fig. 24. The energy spectra of the penetrating iron ions and iron fragments are shown in greater detail in Fig. 25. The shift of the iron fragment spectra to lower energies relative to the surviving beam particles resulting from loss of

Table 2. Benchmark parameters for 1 A GeV iron ions in the four requested materials.

Polyethylene (R₀= 25.3 g/cm²)

Depth (g/cm ²)	$\langle \text{LET} \rangle_{\text{trk}}$ (keV/ μm)	$\langle \text{LET} \rangle_{\text{dose}}$ (keV/ μm)	Dose (nGy)	Fraction Surviving		
				Fe ⁵⁶	Fe ^{55,54}	Total
5	112.9	142.4	180.8	0.50	0.030	0.53
10	92.3	139.2	147.9	0.25	0.032	0.29
15	82.3	143.4	131.9	0.13	0.025	0.15
20	81.1	163.8	129.9	0.067	0.019	0.085
25	98.5	274.9	157.8	0.035	0.0076	0.043
30	33.0	295.7	52.8	0	0	0

PMMA (R₀= 26.1 g/cm²)

Depth (g/cm ²)	$\langle \text{LET} \rangle_{\text{trk}}$ (keV/ μm)	$\langle \text{LET} \rangle_{\text{dose}}$ (keV/ μm)	Dose (nGy)	Fraction Surviving		
				Fe ⁵⁶	Fe ^{55,54}	Total
5	116.1	143.7	186.1	0.54	0.029	0.57
10	96.3	141.0	154.1	0.29	0.032	0.32
15	86.1	144.8	138.0	0.16	0.027	0.19
20	84.7	162.5	135.7	0.088	0.021	0.11
25	116.9	301.7	187.2	0.050	0.015	0.065
30	42.3	334.3	67.8	0	0	0

Aluminum (R₀= 33.9 g/cm²)

Depth (g/cm ²)	$\langle \text{LET} \rangle_{\text{trk}}$ (keV/ μm)	$\langle \text{LET} \rangle_{\text{dose}}$ (keV/ μm)	Dose (nGy)	Fraction Surviving		
				Fe ⁵⁶	Fe ^{55,54}	Total
5	133.3	150.1	213.5	0.78	0.0093	0.79
10	119.2	151.3	191.0	0.61	0.015	0.63
15	109.4	154.6	175.2	0.48	0.017	0.50
20	104.5	162.3	166.7	0.38	0.018	0.40
25	104.5	179.1	167.4	0.30	0.018	0.32
30	120.3	229.9	192.7	0.24	0.017	0.25

Lead (R₀= 50.5 g/cm²)

Depth (g/cm ²)	$\langle \text{LET} \rangle_{\text{trk}}$ (keV/ μm)	$\langle \text{LET} \rangle_{\text{dose}}$ (keV/ μm)	Dose (nGy)	Fraction Surviving		
				Fe ⁵⁶	Fe ^{55,54}	Total
5	147.2	152.0	235.8	0.93	0.0015	0.93
10	144.0	154.3	230.6	0.86	0.0028	0.87
15	141.5	157.3	226.7	0.80	0.0040	0.81
20	139.9	161.5	224.2	0.75	0.0050	0.75
25	139.9	167.3	224.1	0.69	0.0058	0.70
30	141.9	175.8	227.3	0.65	0.0065	0.65

inertia is clearly seen in the graph. Similar observations were made in the neon beam experiments of Schimmerling et al. (Shavers et al. 1993).

SPACEFLIGHT VALIDATION

The present benchmark is a useful exercise for comparison of computational procedures and atomic/nuclear database. The first year of the current project has been mainly focused on advancing computational procedures (Tweed et al. 2005), validation of those procedures (Walker et al. 2005), and providing a sensitivity analysis on the 14,365 nuclear parameters required for space radiation simulations in which 170 isotopes are represented (Heinbockel et al. 2005). This has left little time for improving the physical description of the transport process that is further hampered by the need of a supporting basic nuclear physics research. The main progress is towards implementing multiple Coulomb scattering into the formalism to be followed by off-axis nuclear fragmentation components with a simplified nuclear model. The first issue to be addressed prior to flight validation is the sensitivity of the transport solutions on the nuclear parameters. The theory of nuclear absorption cross sections is well known and new experimental assessments consistently show these cross sections to be within 5 percent or better as new measurements are made (Tripathi et al. 1998,1999, Golovchenko et al. 2002). However, the distribution of the reaction over various reaction channels are less accurately known but experimental knowledge is improving. Since the transport of ions involves the integration of well-understood atomic processes and less well-understood nuclear processes, a parametric sensitivity study to understand the role of nuclear cross section uncertainties is in order. In such a sensitivity analysis, the nuclear absorption cross sections are assumed to be well understood and left unchanged while the specific channel cross section sensitivity will be ascertained.

Although the biological response to HZE exposure is very uncertain, dose equivalent is still assumed a first order approximant of biological injury (NCRP 2001) and will be used herein to study fragmentation cross section sensitivity. The dose equivalent is given as

$$H(x) = K \Sigma_j \int d\Omega dE L_j(E) Q[L_j(E)] \phi_j(x, \Omega, E) \quad (38)$$

where $Q[L_j(E)]$ is the LET dependent quality factor. The particle fields $\phi_j(x, \Omega, E)$ contain uncollided particles and secondary particles which depend on specific reaction cross sections. Of particular importance are the HZE particles with their large LET and associated quality factors providing large contributions to dose equivalent. For example, the Fe ions of the galactic cosmic rays are known to contribute about one third of the total dose equivalent inside space structures (Wilson et al. 1991). We explicitly display the dependence of dose equivalent on the

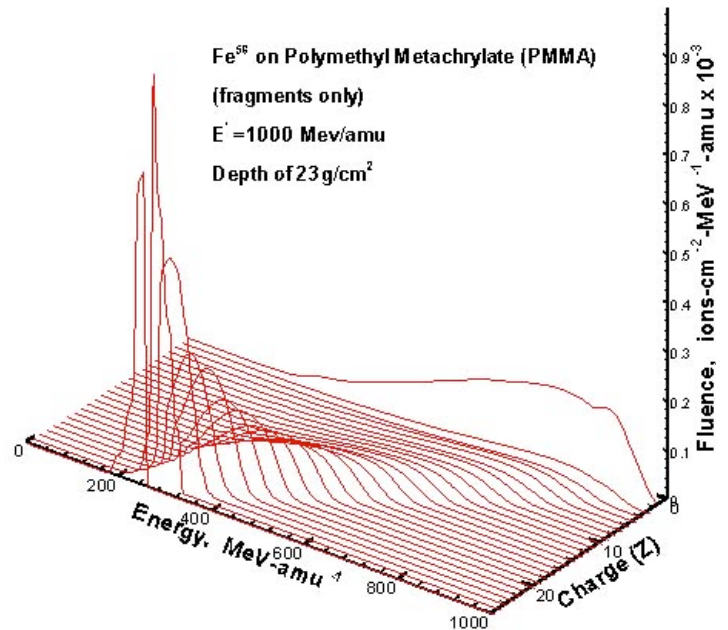


Fig. 24. Iron ion fragment spectra behind 23 g/cm² of PMMA.

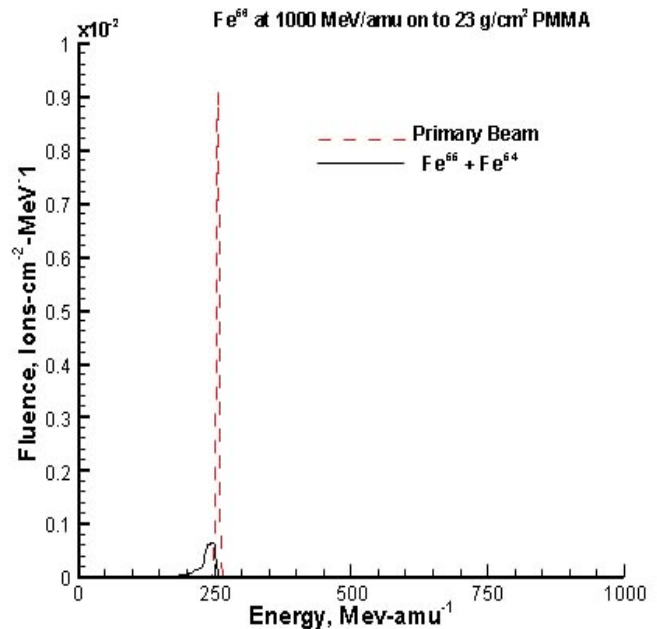


Fig. 25. Iron ion spectra after 23 g/cm² of PMMA.

fragmentation cross sections while suppressing the dependence on x and expand to first order about nominal cross sections given by NUCFRG2 as follows

$$H(\sigma_{jk} + \epsilon_{jk}) = H(\sigma_{jk}) + \partial_{\sigma_{jk}} H(\sigma_{jk}) \epsilon_{jk} \tag{39}$$

where ϵ_{jk} represents the uncertainty in the NUCFRG2 fragmentation cross section σ_{jk} . Note, the term $\partial_{\sigma_{jk}} H(\sigma_{jk})$

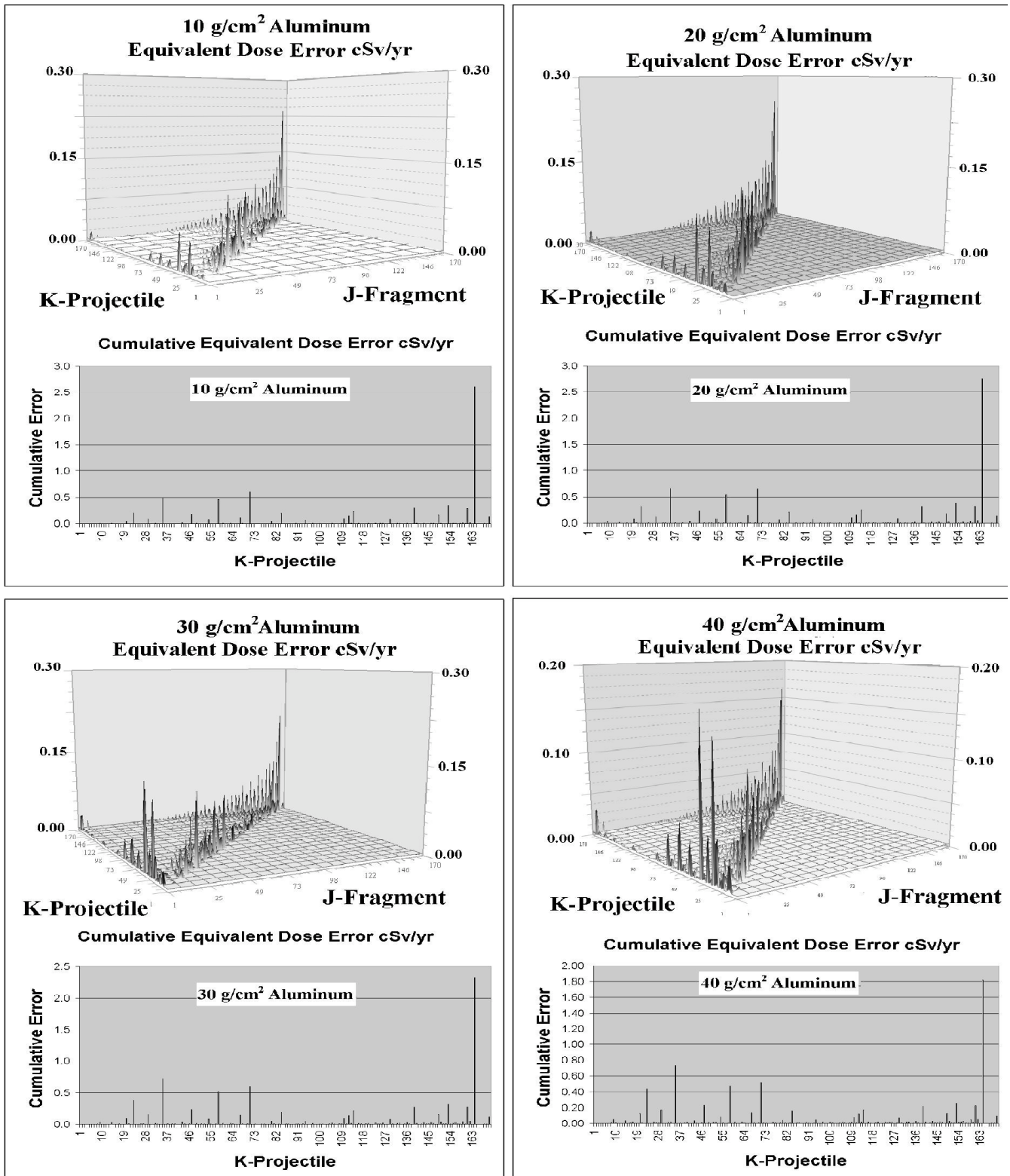


Fig. 26. Error and cumulative error graphs for Aluminum shield at various depths.

represents the sensitivity of H to the variations in the cross section parameter σ_{jk} . Equation (39) has been used as a basis for a study of the uncertainty propagation into the solution as a function of shielding.

The sensitivity coefficient $\partial_{\sigma_{jk}}H(\sigma_{jk})$ is a complicated function of the 14,365 cross sections σ_{jk} and the particles present at the boundary. These are evaluated numerically by finite differencing. It has long been known (Wilson et al. 1997) that only seven ions give over 90 percent of the contributions to dose equivalent: H, He, C, O, Mg, Si, and Fe. Clearly, these ions and their secondaries will play a major role. The sensitivity coefficients $\partial_{\sigma_{jk}}H(\sigma_{jk}) \times \sigma_{jk}$ are shown in Fig. 26. The results shown are for aluminum shielding but other shield compositions are qualitatively similar. The contributions from a single ion type at the boundary is indicated by the sum of contributions of all fragments from the same type of incident ion at the boundary. These are also shown in Fig. 26 by separate panel as the cumulative error for each incident ion type. The essential role of the seven important ions before identified is clear. In the case of iron, the fragments for charge removal up to about 10 are seen as the most important contributors to dose equivalent even up to depths of 40 g/cm². This is due to their abundance and large charge and quality factors. At the larger penetration depths, the light ion fragments from incident iron ions play an increasing role but are dominated by the heavy fragments even at the large depths shown in the figure. The ions of Mg and Si still have significant contributions from fragments with few to several charges removed but the light ions are relatively more important in this case than in the case of iron ions. The ions below Mg have relatively large contributions from the light ion fragments they produce especially at the large depths. It is fortunate that only relatively few fragments of each of relative few incident ions need to be known with a degree of accuracy. We now examine what impact uncertainty in fragmentation cross sections and what level of certainty is required for an adequate solution of the shielding problem.

A cross section uncertainty effects study on the propagated errors in polyethylene, aluminum and copper were performed using the sensitivity data like that in Fig. 26. The propagated error associated with each fragmentation cross section uncertainty is $p \times \partial_{\sigma_{jk}}H(\sigma_{jk}) \times \sigma_{jk}$ where p is a random sequence representing the distribution of propagated uncertainty and chosen from a normal distribution of zero mean and 0.75 standard deviation (a very conservative assumption). The results on the propagated error in the three materials are shown in Fig. 27 as 1- σ error bars for the propagated uncertainties (Heinbockel et al. 2005). The percent rms propagated error is given in Table 3.

Table 3. Propagated percent rms error due to 75 percent uncertainty in ion fragmentation cross sections.

Depth, g/cm ²	Polyethylene	Aluminum	Copper
10	3.49	1.18	0.70
20	3.58	1.85	0.96
30	3.18	2.02	1.39
40	2.00	1.86	1.53

Also shown in Fig. 27 are solutions with all of the σ_{jk} set to zero for comparison. Note, the zero bias and non-systematic assumption leave little uncertainty in the propagated error. We have done systematic error studies which expand the error bars in an unsymmetrical way but still the width of the error bars are minor. It is clear from this result that any added gains in accuracy in fragmentation parameters beyond the NUCFRG2 model will provide minimal improvements to space radiation shield evaluation. However, the continued development of transport procedures and atomic/nuclear database has value in beam characterization for the radiobiology program. The above error propagation analysis will help to make the results of validation with spaceflight data better understood.

There are two principal flight platforms used in the spaceflight validation of the shield analysis codes: the space shuttle and the International Space Station. There is also flight data from space station Mir but the knowledge of the material arrangement on Mir is limited and therefore not used in quantitative analysis. The

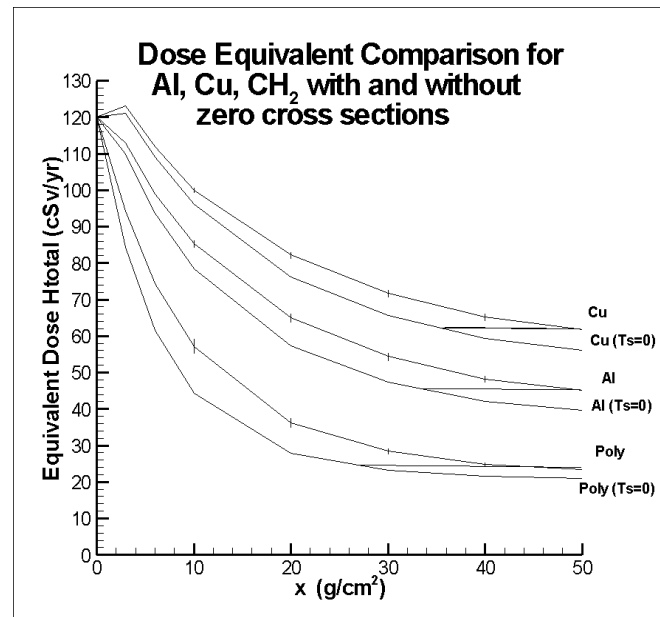


Fig. 27. Nominal dose equivalent and cross section uncertainty comparison with production cross-sections equal to zero ($T_s = 0$).

instrumentation has varied over the time of measurement. Although some preliminary data has been analyzed from the Odyssey Mars Radiation Environment Experiment (MARIE) instrument in Mars orbit, most validation data has been gathered in low Earth orbit (LEO). The space shuttle has well defined geometry models consisting mostly of aluminum alloy 2219 although loading on specific missions which also has well characterized geometry is important in specific mission data (for example, STS-61A the first German Spacelab mission D1). An adequate ISS shield model is developing with the validation of the ISS 7A configuration (Hugger et al. 2003a,b). A historic problem with LEO validation is the uncertainty in the trapped particles (mainly protons). Available proton models denoted AP8 MIN and AP8 MAX were developed to represent the omnidirectional proton flux near solar minimum (circa 1965) and solar maximum (circa 1970). This model uncertainty was partly corrected in STS and ISS dosimetry analysis by adjustments to the trapped flux according to thermoluminescence detector (TLD) readouts. The degree to which AP8 uncertainty enters depends on the orbit inclination and altitude.

The two primary limitations in the LEO trapped environmental models AP8 MIN&MAX as discussed by Wilson et al. (2002d) is the assumption that the trapped particles are isotropic (resulting from the omni-directional fluence description) and poor representation of the dynamic behavior. These omnidirectional models have been relatively successful in describing the radiation environment aboard the highly maneuverable Shuttle wherein anisotropies tend to be averaged. Such models will not be adequate in the formation flying of the ISS mainly oriented in the local horizontal plane along the velocity vector. We have developed a dynamic/anisotropic trapped proton environmental for future use in LEO shield design and operations. These environmental models are placed in a suitable form for evaluation of the incident radiation on the bounding surface of the six-degree of freedom motion of an orbiting spacecraft for shield evaluation (Wilson et al. 2005b). To test the dynamic behavior, we use shuttle TLD data available from 1981 to the present giving good coverage for over two solar cycles. A sample of shuttle TLD measurements and the computational model is given in Table 4. A compilation by Badhwar (Chapter 21 of Wilson et al. 1997) of calculated and observed dose rates in shuttle flight is given in Fig. 28. According to Badhwar (2002), the rms error of both observed and calculated dose rate and dose equivalent rate is less than 15 percent.

Many detector systems are designed to capture some physical quantity such as LET but do so only within the limitations of the detector. Generally we have approached this problem by not comparing to the quantity that the detector is meant to measure but rather to evaluate the detector response to its environment as estimated using shielding models of the platform in which the measurement was made. One such example is the nuclear track detector (CR-39) measurements on the D1 mission of STS-61A. The results of computational models with detector response functions which depend on details of post-flight processing of the exposed detectors as estimated by Shinn et al. (1995) is shown in Fig. 29. Many of the target fragments at the highest LET were not seen by the CR-39 plastic as they were etched away in the track development process but the predicted CR-39 and measured CR-39 responses are good agreement.

A great boon to model validation was the development of the particle detector telescope spectrometer for use on the shuttle (Badhwar et al. 1992, 1994). This high-resolution detector allows detailed testing of spectral

Table 4. Comparison of present model with Shuttle flight data.

Flight	Date	DRNM*	DLOC	TLD† ($\mu\text{Gy/d}$)	Calc. ($\mu\text{Gy/d}$)
STS-41A	11/83	6421	3	64.6	60.8
STS-31	4/90	5701	1	2141	2093
STS-62	3/94	6771	1	94.3	90.7
STS-65	7/94	6822	2	28.3	25.7
STS-82	2/97	7074	1	2978	3014
STS-92	10/00	6417	2	165.9	172.9

* Deep River Neutron Monitor count rate † GCR corrected TLD-100 data

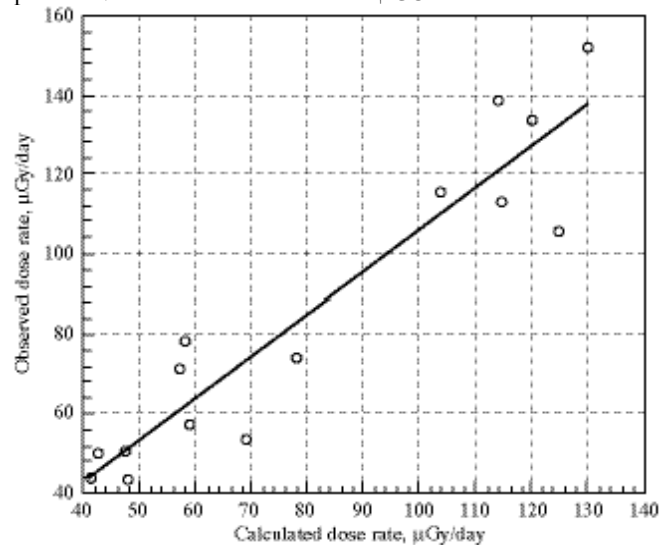


Fig. 28. Observed dose rate versus calculated dose rate (Badhwar, Chapter 21 of Wilson et al. 1997).

components transmitted through or produced in the shuttle hull. Only the more intense components can be detected with sufficient statistical accuracy on the relative short shuttle flights. Figs. 30 and 31 show particles produced in the shuttle hull in the high latitude regions of that particular flight (STS-48) where galactic cosmic rays are present in sufficient intensity although the geomagnetic cutoffs are still relatively high. The particles in the figures represent the secondaries produced in the shuttle hull by much higher energy ions not present in the measurements or the graphs. The older version of HZETRN did not include the direct cluster knockout particles and the figures show mainly decay particles of target nuclei of the shuttle hull material struck by the incoming ions. The revised and current HZETRN include these knockout processes and show excellent agreement with measurements

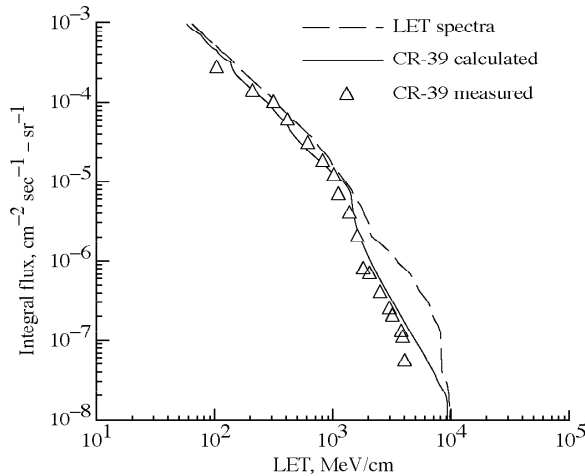


Fig. 29. CR-39 detector response (triangles) compared to predicted CR-39 response and LET spectra during the German Spacelab mission D1 on STS-61A.

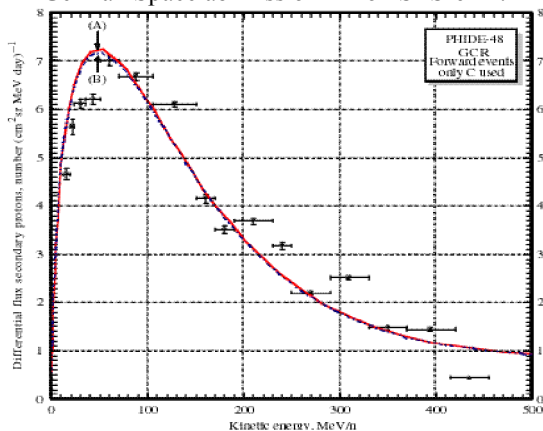


Fig. 30. Comparison of calculated and measured proton spectra on STS-48.

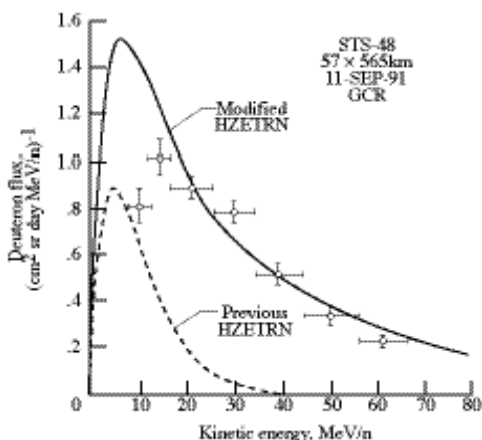


Fig. 31. Comparison of calculated and measured deuteron spectra on STS-48.

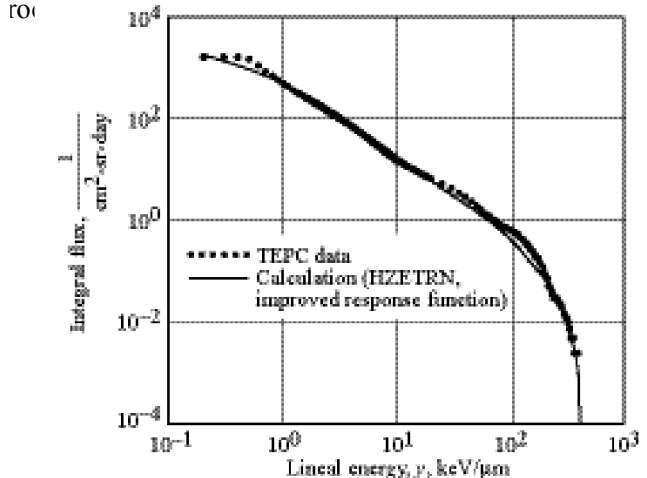


Fig. 32. Galactic cosmic ray induced lineal energy spectrum during STS-57.

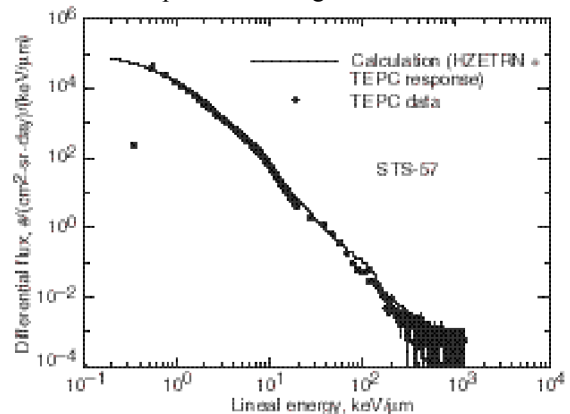


Fig. 33. Trapped proton induced lineal energy spectrum during STS-57.

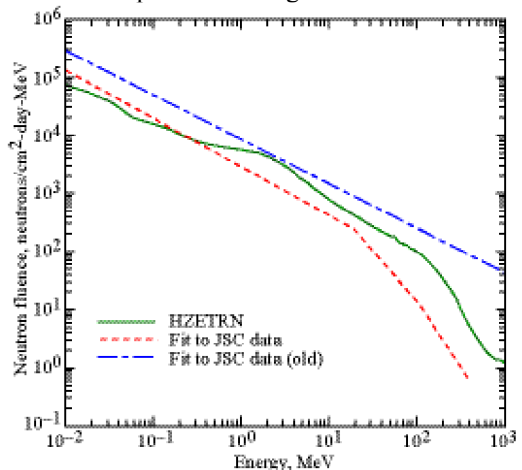


Fig. 34. Comparison of HZETRN with multigroup methods of Cloudsley with the old and new JSC analysis of STS-36 measurements.

and the current HZETRN include these knockout processes showing excellent agreement with the measurements and excellent validation of the light ion production processes.

The Tissue Equivalent Proportional Counter (TEPC) provides spectral distributions of energy deposited within a small volume of gas to approximate the quality of the radiation absorbed (usually represented by LET). The TEPC spectrum is the defined “lineal energy spectrum” as it does not exactly but does somewhat approximates an LET distribution (see Badhwar et al. 1994). The usefulness of this instrument had been limited for many years for lack of a useful model of its response to the space radiations. Shinn et al. (2001) have developed a model for the response of the TEPC used by Badhwar for an estimate of dose equivalent in spaceflight. By developing a model for the response of the TEPC, Shinn et al. hoped to make this instrument more useful in testing shielding models using spaceflight data since flying the TEPC became standard practice on shuttle flights for the last ten years. Further usefulness of the TEPC results from time serial analysis of the measured data to separate the trapped environment from galactic cosmic ray contributions allowing a separate test on shielding against trapped protons and shielding against galactic cosmic rays. Analysis of the environment induced in shuttle flight STS-57 by galactic cosmic rays and by trapped protons as measured and calculated using HZETRN are shown in Figs. 32 and 33. It is expected that the TEPC estimates of dose equivalent will be in good agreement with the computational models as Badhwar has determined.

Limited measurements with a Bonner sphere setup using foil activation methods have been made (Keith et al. 1992) with re-analysis of Keith’s data by Badhwar et al. (2001). The old and new analysis of the Bonner sphere data are shown in Fig. 34 with the revised HZETRN with multigroup methods of Cloudsley et al. (2000). Clearly the computational model is within the uncertainty of the data analysis. Although the results in Fig. 34 are useful in evaluation of computational models, an improved approach would be to calculate the response of the four Bonner spheres from computational models with direct comparison with the foil count rates of the measured sphere data. This would eliminate the need for assumptions as to the

Table 5. Calculated and measured Quality Factors

Organ	Q_{calc}	Q_{meas}
Brain	2.10	1.8±0.1
Colon	2.17	2.0±0.2
Heart	2.15	2.0±0.4
Stomach	2.2	1.7±0.3
Thyroid	1.89	1.7±0.2
Skin _{breast}	2.10	1.8±0.2
Skin _{abdomen}	2.11	1.9±0.2



Fig. 35. The JSC phantom torso as flown on STS-91.

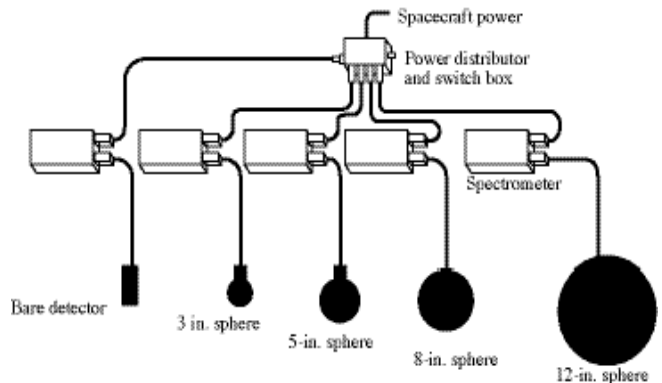


Fig. 36. Apparatus for shield attenuation studies during shuttle flight.

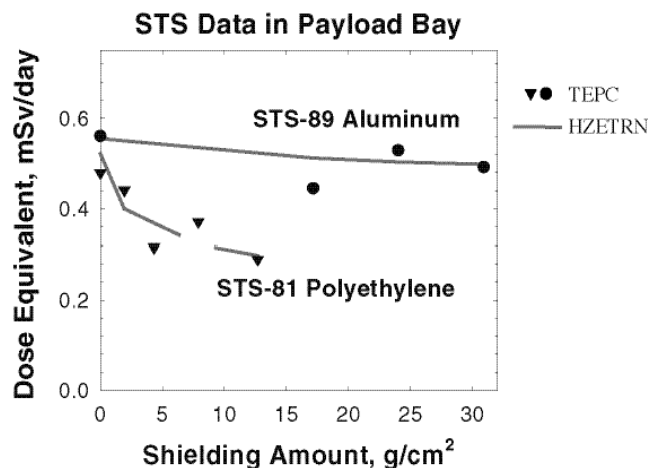


Fig. 37. Experimentally measured and calculated attenuation curves in aluminum and polyethylene in shuttle flight.

neutron spectral components as input to the Bonner sphere analysis methods giving rise to the uncertainties seen in the figure.

Applying radiation shield constraints to the space radiation shield design process requires not only the estimation of the internal spacecraft environment but how that environment is transported in human tissues of a characteristic human shape. To examine this problem a human skeleton (head and torso) is covered with a tissue equivalent plastic and sectioned to allow instrumentation for in-flight measurements (see Fig. 35). The torso phantom was CT scanned to define the geometry for use as a computational model. The instrumentation used TLD, nuclear track foils and TEPCs to allow the mapping of the dose and dose equivalent within the phantom torso model. The instrumented torso phantom was flown on STS-91 followed by data analysis and HZETRN validation. The results of the measurements expressed herein as the average quality factor is given in Table 5. For the listed organs, the calculated dose was within 12 percent of the measurements except for the stomach that was within 19 percent. The cause of the differences was in large part due to need to correct the galactic cosmic ray under-response of the TLDs (Cucinotta personal communication, 2004) and the corrected data was all within 12 percent of the computational models.

The usefulness of the TEPC in evaluating dose equivalent in the space environment being established, Badhwar provided a test rig of five TEPCs (Fig. 36) to study dose equivalent attenuation in the LEO environment. The bare detector allows characterization of the ambient field within the shuttle while the shielded detectors sample the modified environment due the shielding material. A study of LEO radiation attenuation in polyethylene was conducted in the shuttle bay with the doors open on STS-81 and are compared to a similar study of aluminum shielding on STS-89. Note that a direct comparison of aluminum shielding effectiveness to that of polyethylene cannot be made as the two flights are in radically different environments. STS-81 is in a high inclination orbit (51.6°) with large contributions from galactic cosmic radiation, and STS-89 is in a low inclination orbit (28.5°) where the environment is dominated by trapped protons. The results are compared with HZETRN model calculations in Fig. 37. One TEPC failed on STS-89 but it is still clear that good agreement was found between the HZETRN modeled and the measured attenuation curves. This is also true for the STS-81 results for polyethylene shields as shown in the figure. It is clear that polyethylene has superior attenuation characteristics even in environments with large contributions from galactic cosmic radiation (STS-81). As a result, polyethylene is the material of choice for augmenting the ISS shield. Most important is the ability of HZETRN to evaluate correctly the dose equivalent from all components important to human rated systems and provide estimates of ISS

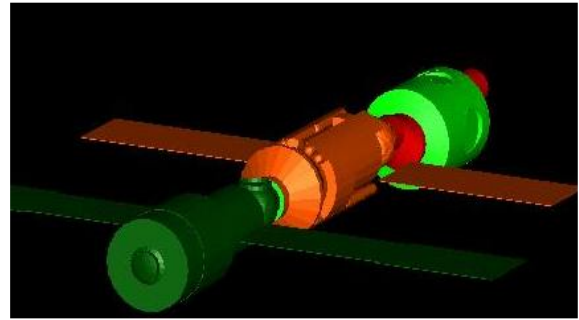


Fig. 38. The ISS 2A.2B Configuration CAD Model.

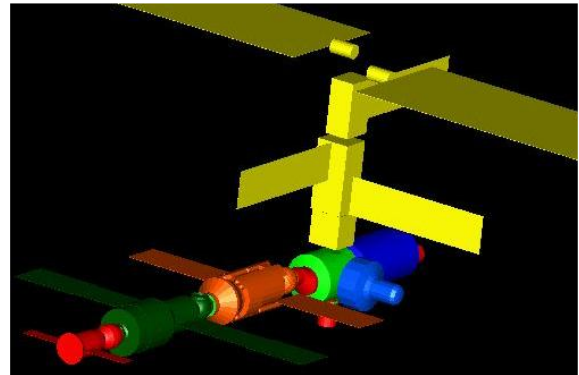


Fig. 39. The ISS 7A Configuration CAD Model.

Table 6. TLD dosimeter locations.

Location	Description
Lab1	Starboard side standoff between starboard and ceiling
Lab2	Near the Lab Window
Lab3	Port side standoff between Deck and Port rack
Lab4	Forward closeout panel starboard upper corner
Lab5	Sleep Station
SM1	Inside Port SM Crew Quarters, Outboard wall aft upper corner
SM2	Inside Starboard SM Crew Quarters - Outboard wall aft upper corner
SM3	Panel 339, aft section behind treadmill- Upper center part of the panel
SM4	Panel 327, overhead, forward of treadmill
SM5	Panel 307 overhead, near center
SM6	Window #14, Transfer Compartment Adapter Section, Starboard Nadir Quadrant

augmentation requirements and value of the benefits.

The omnidirectional models of the trapped environment have been useful for highly maneuverable spacecraft such as the shuttle. For spacecraft like the ISS with its relatively fixed flight attitude in the local vertical reference frame so there is no angle averaging process, the direction of arrival of radiation on the spacecraft exterior is expected to play an important role. The ISS analysis started with use of the dynamic omnidirectional physics based models connected to the conventional AP8 MIN&MAX database environments for 1965 and 1970 respectively (Wilson et al. 2002d)

To create the shielding model, the ISS was re-created using the computer aided design package I-DEAS. The ISS is an on-going endeavor, which has taken the ISS through many stages. To accommodate the changing space station, the CAD shielding model representing the ISS must be re-configurable as well. To do this, the individual components were modeled separately and then combined before analysis into the necessary configuration. All of the components from the first ISS configuration to the current ISS 11A configuration have been modeled. The Components are the Service Module, the Lab Module, the Node 1, the FGB, the 3 Pressurized Mating Adaptors, the Airlock, the Docking Compartment, the Soyuz, and the Truss. For the purpose of this paper, the ISS shielding model needed to represent all of the ISS configurations from the 2A.2B through the 7A. The 2A.2B and 7A configurations are shown in Figs. 38 and 39.

Each ISS component is comprised of multiple parts. In modeling the parts of each component, the focus was on simplicity while trying to maintain the accuracy. Hence, the part's solid angle and thickness relative to the target point had to be preserved (Qualls et al., 1997). To do this, first it was necessary to find out the masses and dimensions of all the objects in an ISS component. For a better description of how individual parts of ISS components were modeled for the ISS shielding model, see Hugger, (2003a).

The initial dose calculation was performed only for the omni-directional trapped radiation case (Wilson et al. 2002d) for the dosimetry locations in Table 6. The anisotropy of the trapped radiation environment was later introduced using the angular dependence in the South Atlantic Anomaly averaged over the ascending and descending node crossings. The GCR environment includes the Earth's shadow in both simulation modes. The six dosimeter locations in the Service Module are shown in Fig. 40. Five of the dose locations (SM-1 to SM-5) are well shielded in all directions. The location SM-6 however is in the pressurized docking adapter with a significant fraction of the modeled shield below 10 g/cm² (Hugger et al. 2003b). The dose along each ray was then calculated by interpolating the amount of shielding within dose versus depth data with specified amount of backing.

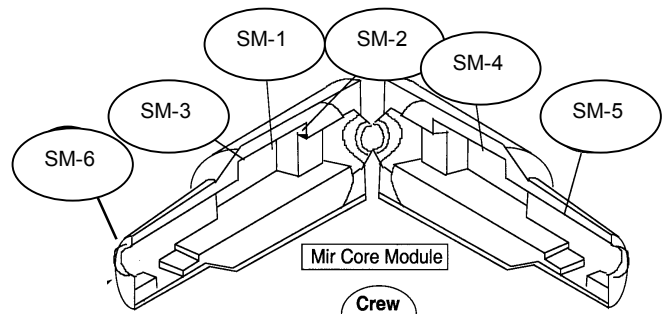


Fig. 40. Dosimeter locations in the ISS Service Module.

Period	Dates	Altitude (km)
Time 1	09/08/00-12/11/00	385.75
Time 2	12/01/00-05/01/01	381.04
Time 3	04/19/01-07/24/01	390.54
Time 4	07/12/01-08/22/01	397.02
2A2B	09/08/01-10/11/01	373.2
3A	10/11/00-10/31/00	389.9
2R	10/31/00-11/30/00	402.8
4A	11/30/00-02/07/01	393.5
5A	02/07/01-04/19/01	398.9
6A	04/19/01-07/12/01	401.8
7A	07/12/01-08/22/01	389.6
7A1	08/10/01-08/22/01	396.8

Table 8. Days for each configuration in a Time Period.

Configuration	Period 1	Period 2	Period 3	Period 4
2A2B	34	-	-	-
3A	20	-	-	-
2R	29	-	-	-
4A	10	69	-	-
5A	-	71	-	-
6A	-	11	84	-
7A	-	-	12	29
7A1	-	-	-	11

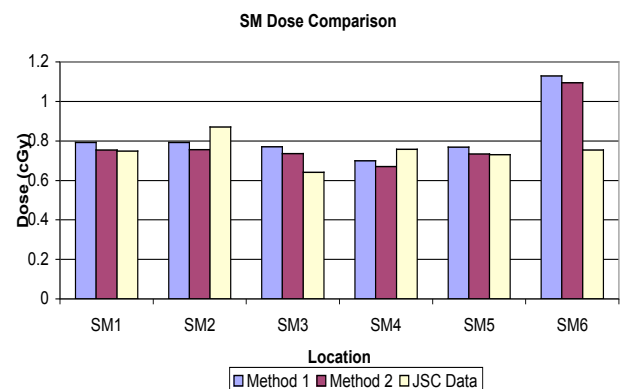


Fig. 41. Comparison of Methods 1 & 2 with JSC flight data measured in the service module.

This process was repeated for all the rays in the thickness file. The total dose was calculated by summing all of the directional doses and then dividing by the total number of directions (depends on normalization).

The measurements took place over four separate time periods using thermo-luminescence detectors (TLD-100) located throughout the ISS. The measurements were performed over the course of nearly 11 months. The dates and time periods for the different measurements are listed in Table 7 with the associated ISS configurations. During these measurements, the ISS was constantly changing configuration, altitudes, and the total number of dosimeters used was changing as well. For the first testing period, there were four TLD's measuring data in the Service Module. The second testing period had 6 TLD's operating in the SM. The third and fourth testing periods utilized all 11 TLD's in the Service and the Laboratory modules. The TLD locations are given in Table 6.

To accurately model the environment for each set of dosimeter data, the altitude and time period were required. The periods labeled Time 1 through Time 4 are periods for accumulating dosimeter data. The altitudes listed in this case are the averages over the as flown five-minute trajectory data. The ISS configurations with associated dates and altitudes were provided by the Johnson Space Center. For each configuration of the ISS, an average altitude was calculated and an environment was generated. There were a total of 8 environments for eight ISS configurations created, also listed in Table 8. The number of days of operation for each configuration within the listed time periods are given in Table 7. For this paper, we will concentrate on time period 4 for which the configuration nearest the current 11A and use various methods for comparing with the TLD dosimeter data. No correction was made for under-response of the TLD to highly ionizing particles, resulting in ~10% underestimate of absorbed dose in water.

The first evaluation method (Method 1) uses the average altitude for the time period 4 but allows evaluation under the two configurations 7A and 7A1. A second method (Method 2) used the altitude apogee and perigee data provided by Johnson Space Center applied to each configuration as given in Table 8 for 7A and 7A1. In each case, the dose was evaluated at each of the six dosimeter points in the Service Module (SM-1 to SM-6) and for five locations in the Laboratory Module (Lab-1 to Lab-5).

Absorbed dose in water calculated for the SM locations using Method 1 & 2 are shown in Fig. 41 in comparison with the dosimetry data measured in the same time period. The TLD dose is used without the small correction for under-response to high LET events. The only difference between methods 1 & 2 is the altitudes used in generating environmental data for the ISS configurations in Table 8. The differences can then be seen as our uncertainty in the actual flight altitudes, and it is highly desirable in further analysis to use as flown flight data. There is reasonable agreement between measurements (generally better than 20 percent) and calculations except for the location SM-6 with its unusually thin shielding. Since the calculation was made using only omnidirectional fluence data it appears that particle

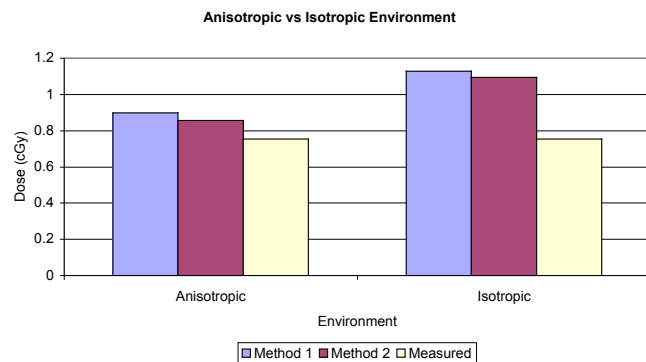


Fig. 42. Anisotropic effects on SM-6 dosimetry.

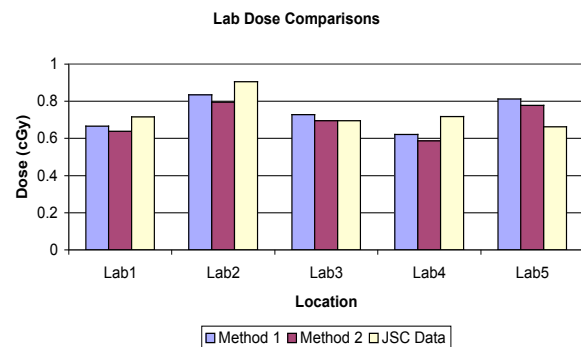


Fig. 43. Comparison of Methods 1 & 2 with JSC flight data measured in the laboratory module.

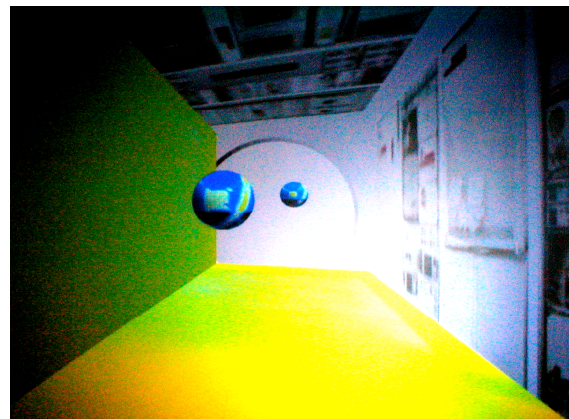


Fig. 44. Directional dose distribution predicted for ISS in passing through South Atlantic Anomaly.

arrival within the thin sections at SM-6 are overestimated by over 45 percent. It is well known that the largest fraction of space exposure comes from the least shielded region.

To test the effects of anisotropy on the SM results, we implemented the directional dependent flux factor as given by Heckman and Nakano (1963). The directional intensity is then defined for direction of arrival defined by the local pitch angle θ and azimuth λ as follows

$$j(\theta, \lambda) = J_{4\pi} C \exp[-(\theta - \pi/2)^2 / 2\sigma_\theta^2] \exp[r_g \cos(I) \cos(\lambda) / h_s] \quad (40)$$

where r_g is the particle gyro-radius about the field line, I is the dip angle, h_s is the atmospheric scale height, σ_θ is the width of the pitch angle distribution, and C is a normalization constant as discussed by Kern (1994). The angular distribution is averaged over the South Atlantic Anomaly crossings for both ascending and descending nodes and the dose at SM-6 re-evaluated. The results are shown in Fig. 42 using both methods 1 and 2 for evaluation of the flux environment. It is clear that anisotropic effects are especially important for this location in the SM.

A preliminary comparison with the Laboratory dosimetry has been made for the five locations Lab-1 to Lab-5 (see Table 6 for locations) during period 4. In this comparison, it is assumed that the trapped radiation is isotropic. The first attempt to compare with the Lab data left two storage racks empty due to lack of data at the time gives mixed results. Addition of 100 pounds of ill-defined “equipment” provides the results in Fig. 43. The agreement is reasonable for this first comparison (all of the data points are within 25%) but treating the anisotropy and the as flown trajectory data may lead to further improvement as it did in the case of the Service Module.

The current status of LEO validation of shield modeling of ISS is encouraging. Clearly, the continued development of an understanding of ISS shield distribution using TLD measurements will require new software able to follow the six degrees of freedom trajectories in environmental evaluation using a fully dynamic and anisotropic trapped particle environment model (Wilson et al. 2005b).

The effects of angular incidence of the LEO environment are shown in Fig. 44 on the directional dose sphere evaluated in the US Habitat module model. On the spheres in Fig. 44, one can clearly see the Earth shadow effects on the GCR arrival as the black region on the bottom of the sphere. The square figure on the front of the sphere results from the low shielding on the space end of the hallway. The diagonal slash is due to the arrival of protons in passage through the South Atlantic Anomaly (SAA). Clearly these features will have a strong influence on how the ISS shielding affects dosimetric measurements. One can not over emphasize the importance of these LEO studies as a test bed for shield design software, as test area for long duration human spaceflight, and as a staging area for future deep space missions.

The current development has a two-fold purpose. First is the evaluation of the ISS shielding model using the ISS dosimeters. This first step is required to validate our understanding on the relation of the ISS distribution of materials on the internal radiation environment. Second is the evaluation of the best means of augmenting the Service Module Crew Quarters to lower the exposure of the crew during ISS operations. In both cases, we anticipate that the angular dependence of the arriving radiation is an important factor.

The importance of angular dependence on ISS dosimeter results has already been demonstrated in some regions of the Service Module as shown for the TLD readings in the Transfer Compartment Adapter Section (SM06 dosimeter location, see Figs. 40 & 45) as shown

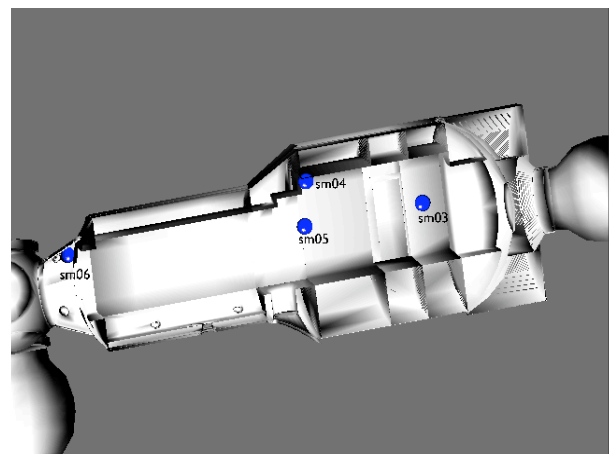


Fig. 45. Cutaway view of Service Module showing dosimeter locations.

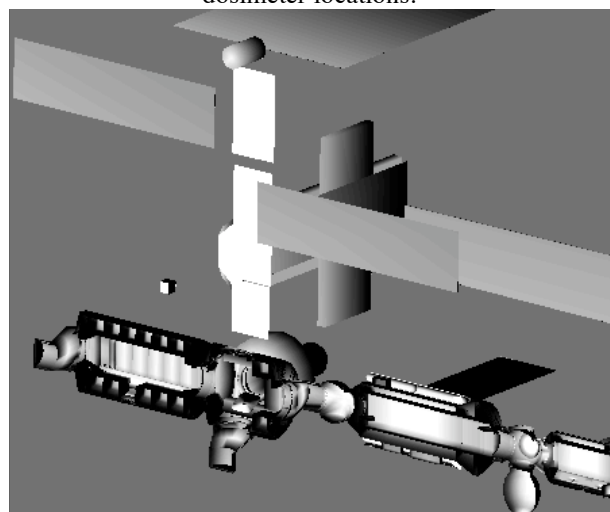


Fig. 46. Cutaway view of ISS 11A.

in Fig. 42. In the figure, we show two methods of evaluating the environment on the basis of conflicting altitude descriptions for both assumed anisotropic and isotropic arrival. Method 1 uses the average altitude over the measurement period and Method 2 uses the apogee and perigee evaluated separately and averaged. Independent of the remaining trajectory issues, it is clear that the anisotropy description is fundamental to understanding the ISS dosimeter data. The current code development will allow not only the inclusion of as flown ISS 3D trajectory data but the inclusion of limit cycle and maneuvers in the environment generation to increase the fidelity of future ISS shield studies. This is critical to evaluation of the ISS 11A shield model shown in Figs. 45 and 46, the future augmentation of the ISS shield, and evaluation of the demonstration flight of the CEV in 2008, and the first uncrewed CEV flight but fully instrumented flight in 2011.

In addition to space flight measurements, the transition of galactic and solar cosmic rays in the Earth's atmosphere has been studied for many decades. Early limitations of state-of-the-art nuclear database generators was a result of comparisons with high altitude balloon flight data gained with gas Cerénkov counters (Webber and Ormes 1967). In these experiments the ion flux of lithium and beyond was measured in the range of 200 A MeV to 5 A GeV with results shown in Fig. 47 in comparison to HZETRN solutions with the original Bowman, Swiatecki and Tsang nuclear model (Bowman et al. 1973) and the modifications of the nuclear excitation energy model by Wilson et al. (1987b). These comparisons were essential to the development of the NUCFRG model. More recently Blattnig, Norbury, and Cucinotta have continued development of pion production models and recently Blattnig and Norbury (Blattnig et al. 2004) have developed a version of HZETRN with meson production and transport and made comparison with atmospheric air shower data as shown in Figs 48 (Blattnig et al. 2005). Although mesons and their decay products play an important role in space radiation interaction with atmospheres where long interaction lengths allow decay into products which have small nuclear cross sections (Abe et al. 2003) and therefore buildup unhindered, the short interaction lengths in condensed materials as a spacecraft have only minor contributions to exposures from mesons (de Angelis et al. 2002). Most important to human space exploration will be their contribution on the mars surface which is now being addressed (Blattnig et al. 2005) for which the validation in Fig. 48 lends confidence in future HZETRN estimates of exposures on the Mars surface.

FUTURE ACTIVITY

The early portion of this activity focused on the multiple charged ion shield code development including the atomic/nuclear database and transport procedures. As the early versions of these HZE transport codes matured (Wilson et al. 1987a, 1987b) a separate code for proton/neutron transport was developed by a grant under the Historically Black College and University grant program at Hampton University. This code first needed a realistic nuclear database (Wilson et al. 1988a, 1988c) for the development of computational procedures that

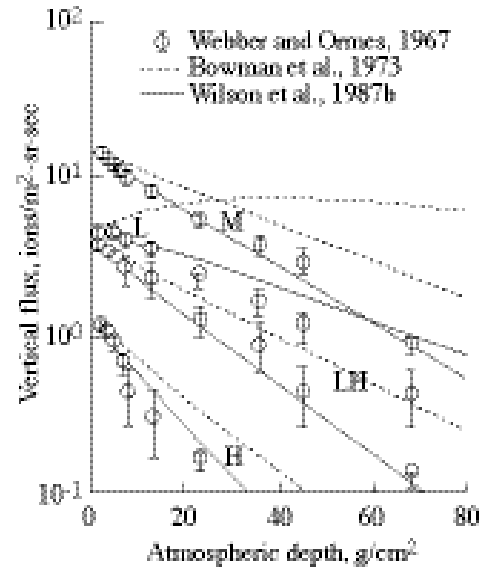


Fig. 47. Cosmic ray transition curves above 300 A MeV measured by Webber and Ormes (1967).

the ion flux of lithium and beyond was measured in the range of 200 A MeV to 5 A GeV with results shown in Fig. 47 in comparison to HZETRN solutions with the original Bowman, Swiatecki and Tsang nuclear model (Bowman et al. 1973) and the modifications of the nuclear excitation energy model by Wilson et al. (1987b). These comparisons were essential to the development of the NUCFRG model.

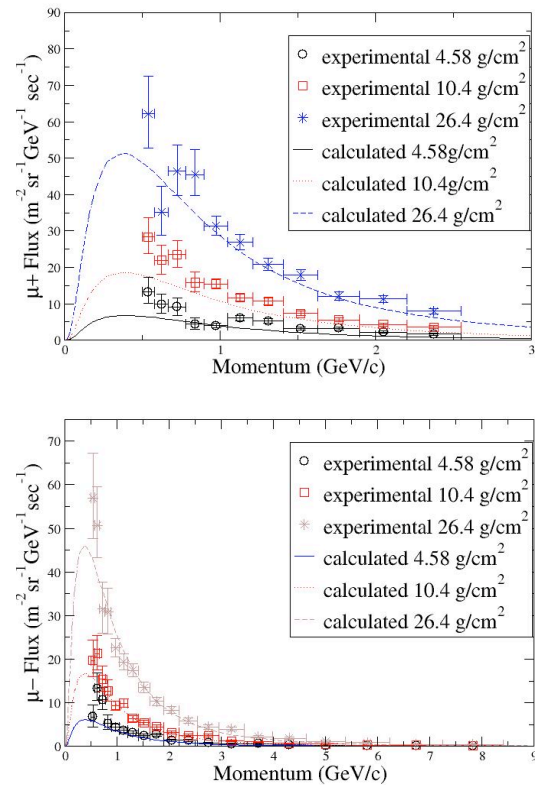


Fig. 48. Calculated muon spectra (top panel μ^+ , bottom panel μ^-) for three heights in Earth's atmosphere compared with experimental results from BESS2001 (Abe et al. 2003).

could be seamlessly integrated with the HZE transport code using marching procedures (Wilson et al. 1991). With the improvement of the light ion transport procedures including the cluster knockout processes (Cucinotta 1993) the first generation of HZETRN was finalized (Wilson et al. 1995b) with the preliminary proton/neutron and light ion database. Among various improvements for the HZETRN, we unsuccessfully proposed improving the proton/neutron database as a critical issue in space shielding estimates but the proposal was rejected. Even in this new round of research and development, only transport code method development was funded with no support for nuclear database development. Since transport code development requires an adequate nuclear database some nuclear model investments are made on a time available basis. Such an example is the pion production database developed by Steve Blattmig and John Norbury at the University of Wisconsin and the associated modified version of HZETRN (Blattmig et al. 2004) giving the results shown in Fig. 48. Under this new transport code development activity, the development of a fully 3-D computational procedure is being studied but with the preliminary nuclear models with minor modifications derived from “as-time-available” activity. A recent comparison of methods and databases is shown in Fig. 49 including a forward/backward multigroup method (Clowdsley 2000), a Pn multigroup implementation (Heinbockel et al. 2003), an Sn coupled HZETRN approximation (Singleterry et al. 1998), and MCNPX solution for the neutron fluence generated by the February 23, 1956 solar particle event in aluminum. The forward/backward multigroup method (Fb) and polynomial expansion method (Pn) utilize the HZETRN database while the Sn and MCNPX utilize their own database. The fact that the similar results are found for the Fb and Pn methods indicates the most pressing problem is the nuclear database utilized in the HZETRN affecting the neutron transport.

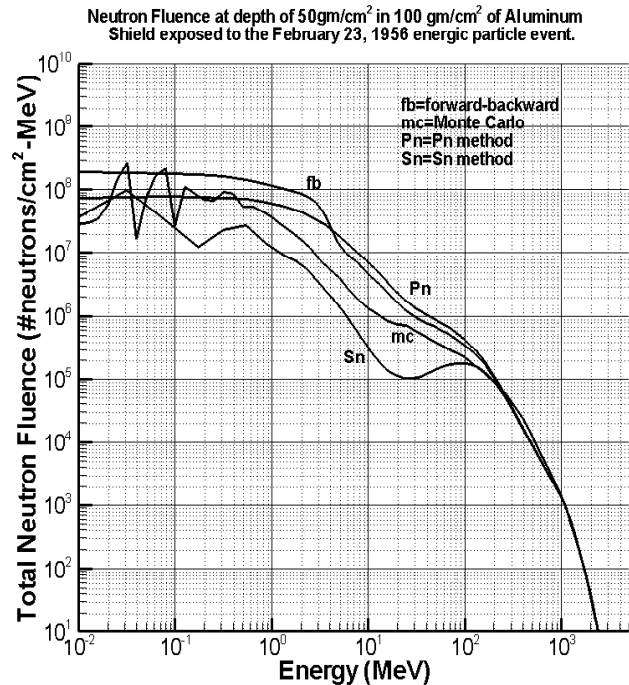


Fig. 49. Total neutron fluence at 50 g/cm² depth of in a 100 g/cm² aluminum shield exposed to the fluence of the February 23, 1956 Solar particle event.

SUMMARY

In the present report, we have reviewed the status of the basic physics models and solution techniques for space radiation transport through materials and spacecraft of interest. This is followed by a review of the verification and validation (V&V) procedures used in code development. Since the V&V activity was applied during code as test to new sections of code, it is not a uniform work since differing stages of development were used. The final assessment of the marching version of the codes circa 1995 and later are mainly for the code as it stood after the end of the funding period for code development and so the code at that time has only seen changes in the neutron propagator. A satisfactory neutron propagator must await an improved nuclear data base development to be finalized. Even so the estimate of dosimetric quantities are judged to be uncertain by only 15 percent by workers at the Johnson Space Center and the basis of this assessment is partly presented in the validation work within this paper. Future work will emphasize both laboratory and space validation resulting in a flexible code useful not only to the design engineer but to the radiobiologist in their studies as well.

REFERENCES

- Abe, K., Sanuki, T., Anraku, K. et al. Measurement of protons, helium and muon spectra at small atmospheric depths with BESS spectrometer. *Phys. Lett. B* 564: 8-20; 2003.
- Alsmiller, R.G. High-Energy Nucleon Transport and Space Vehicle Shielding, *Nucl. Sci. & Eng.* 27: 158-189; 1967.
- Anderson, B.M., Wilson, J.W., Nealy, J.E., Badavi, F.F., Aiello, J. *Jovian icy moon Excursions: Radiation fields, microbial survival and bio-contamination study.* SAE 2004-01-2327, 2004.

- Armstrong, T.W., Colburn, B.L. Predictions of secondary neutrons and their importance to radiation effects inside the international space station. *Radiat. Meas.* 33: 229-234; 2001.
- Badhwar, G.D., Konradi, A., Hardy, A., Braby, L.A. Active dosimetric measurements on shuttle flights. *Nucl. Tracks and Radiat. Meas.* 20: 13-20; 1992.
- Badhwar, G.D., Cucinotta, F.A., Braby, L.A., and Konradi, A. Measurements on the shuttle of the LET spectra of galactic cosmic radiation and comparison with the radiation transport model, *Radiat. Res.*, vol. 139: 344-351; 1994.
- Badhwar, G.D., et al. Neutron measurements onboard the space shuttle. *Radiat. Meas.* 33:235-241; 2001
- Badhwar, G.D., Atwell, W., Badavi, F.F., Yang, T.C., Cleghorn, T.F. Space radiation absorbed dose distribution in a human phantom, *Radiat. Res.* 157: 76-91, 2002.
- Bertini, H.W., Guthrie, M.P., Culkowski, A.H. *Nonelastic Interactions of Nucleons and π -Mesons with Complex Nuclei at Energies Below 3 GeV*. ORNL TM-3148, 1972.
- Blattnig, S.R., Norbury, J.W., Norman, R.B., Wilson, J.W., Singleterry, R.C., Tripathi, R.K. *MESTRN: A Deterministic Meson-Muon Transport Code for Space Radiation*. NASA/TP-2004-212995, 2004.
- Blattnig, S.R., de Angelis, G., Badavi, F.F., Norman, R.B., Norbury, J.W. Preliminary Analysis of Pion and Muon Radiation on Mars. *Adv. Space Res.* (2005, In press)
- Bowman, J.D., Swiatecki, W.J., Tsang, C.F. *Abrasiou and Ablation of Heavy Ions*. LBL-2908, Lawrence Berkeley Lab. Univ. of California, 1973.
- Cloudsley, M.S., et al. A comparison of the multigroup and collocation methods for solving the low-energy neutron Boltzmann equation. *Can. J. Phys.* 78: 45-56; 2000.
- Cloudsley, M.S. et al. *Shuttle Induced Neutron Environment: Computational Requirements and Validation*. International Conference on Environmental Systems, SAE 2002-01-2460, 2002.
- Cucinotta, F. A.; Hajnal, F.; and Wilson, J. W.: Energy Deposition at the Bone-Tissue Interface from Nuclear Fragments Produced by High-Energy Nucleons. *Health Physics* 59: 819-825;1990.
- Cucinotta, F. A.; Katz, R.; Wilson, J. W.; Townsend, L. W.; Shinn, J. L.; and Hajnal, F. Biological Effectiveness of High-Energy Protons: Target Fragmentation. *Radiat. Res.* 127:130-137; 1991.
- Cucinotta, F. A. *Calculations of cosmic ray helium transport in shielding materials*, NASA TP-3354, 1993.
- Cucinotta, F. A., and R. R. Dubey, Alpha-Cluster Description of Excitation Energies in ^{12}C (^{12}C , 3α) X at 2.1A GeV, *Phys. Rev.*, C50: 979-984; 1994.
- Cucinotta, F. A.; Wilson, J. W.; Shinn, J. L.; and Tripathi, R. K: Assessment and Requirements of Nuclear Reaction Data Bases for GCR Transport in the Atmosphere and Structures, *Adv. Space Res.*, 21(12): 1753-1762 1998.
- Cucinotta, F.A., Saganti, P.B., Hu, X., Kim, M.-H. Y., Cleghorn, T.F., Wilson, J.W., Tripathi, R.K., Zeitlin, C.J. *Physics of the Isotopic Dependence of Galactic Cosmic Ray Fluence behind Shielding*. NASA/TP-2003-210792, 2003.
- De Angelis, G., Wilson, J.W., Cloudsley, M.S., Nealy, J.E., Humes, D.H., and Clem, J.M. Lunar Lava Tubes Radiation Safety Analysis, *J. Rad. Res.*, 43: Suppl., S41-S45; 2002.
- Ganapol, B.D.; Townsend, L.W.; Lamkin, S.L.; Wilson, J.W.: *Benchmark solution for the galactic heavy ion transport equations with energy and spatial coupling*. NASA TP-3112, October 1991.
- Golovchenko, A.N., Skvarc, J., Yasuda, N., Giacomelli, M., Tretyakova, S.P., Ilic, R., Bimbot, R., Toulemonde, M., Murakami, T. Total charge-changing and partial cross-section measurements in the reactions of ~ 110 -250 MeV/nucleon ^{12}C in carbon, paraffin, and water. *Phys. Rev. C* 66:014609; 2002.
- Heckman, H.H., Nakano, G.H. East-west asymmetry in the flux of mirroring geomagnetic trapped protons. *J. Geophys. Res.* 68:2117-2120; 1963.
- Heinbockel, J.H., Feldman, G.D., Cloudsley, M.S., Wilson, J.W., Singleterry, R.C. *Solutions to the Low Energy Neutron Boltzmann Equation*. International Conference on Environmental Systems. SAE 2003-01-2339, 2003.
- Heinbockel, J.H., et al. Cross Section Sensitivity Analysis and Propagated Errors in HZE Exposures. *Radiat. Meas.* In press, 2005.
- Hugger, C.P. et al. ISS as a platform for environmental model evaluation. *Space Technology and Applications International Forum-STAIF 2003*, AIP Conference Proceedings, vol. 654, pp 1011-1017, 2003a.
- Hugger, C.P., Nealy, J.E., Cloudsley, M.S., Wilson, J.W., Qualls, G.D., Atwell, W., Cucinotta, F.A., Golightly, J.J., Semones, E., Shavers, M.R. *Preliminary Validation of an ISS Radiation Shielding Model*. AIAA 2003-6220, 2003b.

- Keith, J.E., Badhwar, G.D., Lindstrom, D.J. Neutron spectrum and dose-equivalent in Shuttle flights during solar maximum. *Nucl. Tracks & Radiat. Meas.* 20:41-47; 1992.
- Kern, J.W. A note on vector flux models for radiation dose calculations. *Radiat. Meas* 23: 43-48; 1994.
- Kim, M.; Wilson, J. W.; Kiefer, R. L.; and Thibeault, S. A.: *Effects of Isotope Selection on Solution Convergence in HZE Transport*. NASA TP-3445, 1994.
- NCRP, National Council on Radiation Protection & Measurements, *Radiation Protection Guidance for Activities in Low Earth Orbit*. NCRP Report 132, 2001.
- Nealy, J.E., Anderson, B.M., Cucinotta, F.A., Wilson, J.W., Katz, R., Chang, C.K. *Transport of Space Environment Electrons: a Simplified Rapid-Analysis Computational Procedure*. NASA/TP-2002-211448, 2002.
- Olson, D. L., B. L. Berman, D. E. Greiner, H. H. Heckman, P. J. Lindstrom, and H. J. Crawford, Factorization of Fragment-Production Cross Sections in Relativistic Heavy-Ion Collisions, *Phys. Rev.*, C28: 1602–1613; 1983.
- Pinsky, L., Carminati, F., Ferrari, A. Simulation of space Shuttle neutron measurements with FLUKA. *Radiat. Meas.* 33: 335-339; 2001.
- Qualls, G.D. and Boykin, R. Space Radiation Shielding Analysis by CAD Techniques. Chapter 17 of NASA CP-3360, 1997.
- Qualls, G.D., et al. International Space Station Radiation Shielding Model Development. *International Conference on Environmental Systems*, 2001-01-2370, 2001.
- Qualls, G.D., Wilson, J. W., Cucinotta, F.A., Nealy, J.E., Hugger, C.P., Atwell, W., and Shavers, M. International Space Station Radiation Shield Augmentation Optimization. *Space 2003 Conference*, AIAA 2003-6222.
- Ranft, J. The FLUKA and KASPRO Hadronic Cascade Codes. *Computer Techniques in Radiation Transport and Dosimetry*, W. R. Nelson and T.M. Jenkins, eds, Plenum Press, pp. 339-371, 1980.
- Schall, I., *Untersuchung der Kernfragmentation Leichter Ionen im Hinblick auf die Strahlentherapie*. Dissertation, Technischen Hochschule Darmstadt, 1994.
- Schardt, D., I. Schall, H. Geissel, H. Irnich, G. Kraft, A. Magel, M. F. Mohar, G. Münzenberg, F. Nickel, C. Scheidenberger, W. Schwab, and L. Sihver, Nuclear Fragmentation of High-Energy Heavy Ions in Water, *Adv. Space Res.* 17 (1995).
- Schimmerling, W., Rapkin, M., Wong, M., Howard, J. The propagation of relativistic heavy ions in multielement beam lines. *Medical Phys.* 13: 217-228; 1986.
- Shavers, M. R., Curtis, S.B., Miller, J., Schimmerling, W. The fragmentation of 670A MeV Neon-20 as a function of depth in water. II. One-generation transport theory. *Radiat. Res.* 124: 117-130; 1990.
- Shavers, M. R., Frankel, K., Miller, J., Schimmerling, W., Townsend, L. W., Wilson, J. W., The Fragmentation of 670 A MeV Neon-20 as a Function of Depth in Water. III. Analytic Multigeneration Transport Theory. *Radiat. Res.*, 134(1): 1-14; 1993.
- Shavers, M.R., Cucinotta, F.A., and Wilson, J.W., HZETRN: neutron and proton production in quasi-elastic scattering of GCR heavy-ions. *Radiat. Meas.* 33, 347-354, 2001.
- Shinn, J. L.; Wilson, J. W.; Badavi, F. F.; Benton, E. V.; Csige, I.; Frank, A. L.; and Benton, E. R.: HZE Beam Transport in Multilayered Materials. *Radiat. Meas.*, 23: 57-64; 1994.
- Shinn, J.L., Cucinotta, F.A., Wilson, J.W., Badhwar, G.D., O'Neill, P.M., Badavi, F.F. Effects of target fragmentation on evaluation of LET spectra from space radiations in low earth orbit (LEO) environment—Impact on SEU predictions, *IEEE Trans. Nucl. Sci.*, 42: 2017–2025; 1995.
- Shinn, J.L., Cucinotta, F.A., Simonsen, L.C., Wilson, J.W., Badavi, F.F., Badhwar, G.D., Miller, J., Zeitlin, C., Heilbronn, L., Tripathi, R.K., Cloudsley, M.S., Heinbockel, J.H., Xapsos, M.A. “Validation of a Comprehensive Space Radiation Transport Code”, *IEEE Transactions on Nuclear Science*, 45: 2711-2719; 1998.
- Shinn, J.L., Wilson, J.W., Xapsos M.A. *An improved analytical model for microdosimeter response*. NASA/TP-2001-211040, 2001.
- Sihver, L., C. H. Tsao, R. Silberberg, A. F. Barghouty, and T. Kanai, Calculations of Depth-Dose Distributions, Cross Sections, and Momentum Loss, *Adv. Space Res.*, 17; 1995.
- Silberberg, R.; Tsao, C.H.; Shapiro, M.M. Semiempirical Cross Sections, and Applications to Nuclear Interactions of Cosmic Rays. *Dpsllsyion znuvlrst Trsvyiond snf Their Applications*, B.S.P. Shen and M. Merker, eds., D. Reidel Publ. Co pp. 49-81, 1977.

- Singleterry, R. C.; and Wilson; J. W.: Angular Neutron Transport Investigation in the HZETRN Free-space Ion and Nucleon Transport and Shielding Computer Program, *Advancements and Applications in Radiation Protection & Shielding*, Nashville, TN, April 19-23, 1998.
- Singleterry, R.C. et al. *Collaborative Engineering Methods for Radiation Shield Design. International Conference on Environmental Systems*, SAE 2001-01-2367, 2001.
- Tripathi, R.K., Townsend, L.W., Kahn, F. Role of intrinsic width in fragment momentum distributions in heavy ion collisions, *Phys. Rev. C.*, 48(4), R1775-R1777; 1994.
- Tripathi, R.K; Wilson, J.W.; Cucinotta, F.A; "Nuclear Absorption Cross Sections using Medium Modified Nucleon-Nucleon Amplitudes"; *Nucl. Instru. and Meth. in Phys. Res. B (NIMB)*, 145: 277-282; 1998.
- Tripathi, R.K; Cucinotta, F.A; Wilson, J.W.; "Medium Modified Nucleon-Nucleon Cross Sections in a Nucleus"; *Nucl. Instru. and Meth. in Phys. Res. B (NIMB)*, 152: 425-431, 1999.
- Tull, C. E., *Relativistic Heavy Ion Fragmentation at HISS*, University of California, LBL 29718, Oct. 1990.
- Tweed, J. et al. *Validation of a Radiation Transport Model for a Shield and Solid State Detector Arrangement*. AIAA-2003-6256, 2003.
- Tweed, J., Walker, S.A., Wilson, J.W., Cucinotta, F.A., Tripathi, R.K., Blattinig, S., Mertens, C.J. Computational Methods for the HZETRN Code. *Adv. Space Res.* In press, 2005.
- VerHage, J.E., Sandridge, C.A., Qualls, G.D., Rizzi, S.A., ISS Radiation Shielding and Acoustic Simulation Using an Immersive Environment, *Immersive Projection Technology 2002 Symposium*, March 24-25, 2002, Orlando, FL.
- Walker, S.A., Tweed, J., Wilson, J.W., Cucinotta, F.A., Tripathi, R.K., Blattinig, S., Zeitlin, C., Heilbronn, L., Miller, J. Validation of the HZETRN Code for Laboratory Exposures with 1 A GeV Iron Ions in Several Targets. *Adv. Space Res.* In press, 2005.
- Webber, W.R., Ormes, J.F., Cerenkov-Scintillation Counter Measurements of Nuclei Heavier than Helium in the Primary Cosmic Radiation. 1. Charge Composition and Energy Spectra Between 200 MeV/Nucleon and 5 beV/Nucleon. *J. Geophys. Res.—Space Phys.* 72:5957-5976; 1967.
- Wilson, J.W., Khandelwal, G.S. Proton dose approximation in convex geometry. *Nucl. Tech.* 23: 298-305;1974.
- Wilson, J.W., Lamkin, S.L. Perturbation theory for charged-particle transport in one dimension. *Nuclear Sci & Eng.* 57:292-299; 1975.
- Wilson, J.W. *Analysis of the theory of high-energy ion transport*. NASA TN D-8381, 1977.
- Wilson, J.W., Townsend, L.W., Bidasaria, H.B., Schimmerling, W., Wong, M. Howard, J. 20-Ne depth-dose relations in water. *Health Phys.* 46: 1101-1111; 1984.
- Wilson, J. W., Badavi, F. F., Methods of Galactic Heavy Ion Transport. *Radiat. Res.* 108: 231; 1986.
- Wilson, J. W.; Townsend, L. W.; and Badavi, F. F.: A Semiempirical Nuclear Fragmentation Model. *Nucl. Inst. & Methods* B18: 225; 1987a.
- Wilson, J. W.; Townsend, L. W.; and Badavi, F. F.: Galactic Cosmic Ray Propagation in Earth's Atmosphere. *Radiat. Res.* 109: 173-183; 1987b.
- Wilson, J.W., Badavi, F.F., Townsend, L.W. A benchmark for galactic cosmic ray transport codes. *Radiat. Res.* 114: 201-206; 1988a.
- Wilson, J.W. S. Y. Chun, W. W. Buck, and L. W. Townsend: High Energy Nucleon Data Bases. *Health Phys.*, 55: 817-819; 1988b.
- Wilson, J. W., Townsend, L. W., Chun, S. Y., Buck, W. W., Khan, F., Cucinotta, F. A. *BRYNTRN: A Baryon Transport Code*. NASA TM-4037, June 1988c.
- Wilson, J. W., Townsend, L. W., Schimmerling, W., Khandelwal, G. S., Khan, F., Nealy, J. E., Cucinotta, F. A., Simonsen, L. C., Shinn, J. L., Norbury, J. W. *Transport Methods and Interactions for Space Radiations*. NASA RP-1257, 1991.
- Wilson, J. W., Shavers, M. R., Badavi, F. F., Miller, J., Shinn, J. L., and Costen, R. C., Nonperturbative Methods in HZE Propagation. *Radiat. Res.* 140: 241-244; 1994a.
- Wilson, J. W., Townsend, L. W., Shinn, J. L., Badavi, F. F., Lamkin, S. L., Galactic Cosmic Ray Transport Methods: Past, Present, and Future. *Adv. Space Res.* 14: (10) 841 - (10) 852, 1994b.
- Wilson, J. W., R. K. Tripathi, F. A. Cucinotta, J. L. Shinn, F. F. Badavi, S. Y. Chun, J. W. Norbury, C. J. Zeitlin, L. H. Hielbronn, and J. Miller, NUCFRG2, *An Evaluation of the Semiempirical Nuclear Fragmentation Database*, NASA TP-3533, 1995a.
- Wilson, J. W.; Badvi, F. F.; Cucinotta, F. A.; Shinn, J. L.; Badhwar, G. D.; Silberberg, R.; Tsao, C. H.; Townsend, L. W.; and Tripathi, R. K.: HZETRN: *Description of a Free-Space Transport and Shielding Program*. NASA TP-3495, May 1995b.

- Wilson, J.W., Miller, J.W., Konradi, A., Cucinotta, F.A. *Shielding Strategies for Human Space Exploration*. NASA CP-3360, 1997.
- Wilson, J. W., Cucinotta, F. A., Tai, H., Shinn, J. L., Chun, S. Y., Tripathi, R.K., Sihver, L. Transport of light ions in matter. *Adv. Space Res.* 21(12): 1763-1771; 1998.
- Wilson, J.W., Tripathi, R.K., Qualls, G.D., Cucinotta, F.A., Prael, R.E., Norbury, J.W., Heinbockel, J.H., Tweed, J., de Angelis, G. Advances in Space Radiation Shielding Codes, *J. Rad. Res.* 43: Suppl., S87-S91; 2002a.
- Wilson, J.W., Tweed, J., Tai, H., and Tripathi, R.K. A simple model for straggling evaluation. *Nucl Inst & Methods B* 194: 389-392; 2002b.
- Wilson, J.W., Korte, J.J., Heinbockel, J.H., Cloudsley, M.S., Badavi, F.F., Troung, A.: *Ionizing radiation shielding: Multifunctionality and MDO processes*. SAE 2002-01-2334, 2002c.
- Wilson, J.W. et al., *Natural and Induced Environment in Low Earth Orbit*. NASA/TM-2002-211668, 2002d.
- Wilson, J.W., Korte, J.J., Sobieski, J., Badavi, F.F., Chokshi, S.M., Martinovic, Z.N., Cerro, J., Qualls, G.D. Radiation Shielding, MDO Processes, and Single Stage to Orbit Design. *AIAA Space 2003 conference*, AIAA 2003-6259.
- Wilson, J.W., Cucinotta, F.A., Schimmerling, W. Emerging Radiation Health-Risk Mitigation Technologies. *Space Technology Applications & Information Forum*, STAIF-2004, AIP Conference Publications, 2004a.
- Wilson, J.W., Tripathi, R.K., Qualls, G.D., Cucinotta, F.A., Prael, R.E., Norbury, J.W., Heinbockel, J.H., and Tweed, J.: A Space Radiation Transport Methods Development, *Adv. Space Res.* 34: 1319-1327; 2004b.
- Wilson, J.W., Tweed, J., Walker, S.A., Cucinotta, F.A., Tripathi, R.K., Blattnig, S., Mertens, C.A. A Benchmark for Laboratory Exposures with 1 A GeV Iron Beams. *Adv. Space Res.* (in press 2005a)
- Wilson, J.W., Cucinotta, F.A., Golightly, M.J., Nealy, J.E., Qualls, G.D., Badavi, F.F., de Angelis, G., Anderson, B.M., Cloudsley, M.S., Luetke, N., Zapp, N., Shavers, M.R., Semones, E., Hunter, A. International Space Station: A Testbed for Experimental and Computational Dosimetry. *Adv. Space Res.* (In press, 2005b).
- Wong, M., Schimmerling, W., Phillips, H., Ludewigt, B.A., Landis, D., Walton, J., Curtis, S.B. The multiple coulomb scattering of very heavy charged particles. *Medical Phys.* 17(2):163-171; 1989.
- Zeitlin, C., Heilbronn, L., Miller, J., Rademacher, S.E., Borak, T., Carter, T.R., Frankel, K.A., Schimmerling, W., Stronach, C.E. Heavy fragment production cross sections from 1.05 GeV/nucleon ^{56}Fe in C, Al, Cu, Pb, and CH₂ targets. *Phys. Rev.* C56: 388-397; 1997.
- Zeitlin, C., Heilbronn, L., Miller, J. Detailed characterization of the 1087 MeV/nucleon ^{56}Fe beam used for radiobiology at the AGS. *Radiat. Res.* 149, 560-569, 1998.

REPORT DOCUMENTATION PAGE			Form Approved OMB No. 0704-0188		
<p>The public reporting burden for this collection of information is estimated to average 1 hour per response, including the time for reviewing instructions, searching existing data sources, gathering and maintaining the data needed, and completing and reviewing the collection of information. Send comments regarding this burden estimate or any other aspect of this collection of information, including suggestions for reducing this burden, to Department of Defense, Washington Headquarters Services, Directorate for Information Operations and Reports (0704-0188), 1215 Jefferson Davis Highway, Suite 1204, Arlington, VA 22202-4302. Respondents should be aware that notwithstanding any other provision of law, no person shall be subject to any penalty for failing to comply with a collection of information if it does not display a currently valid OMB control number.</p> <p>PLEASE DO NOT RETURN YOUR FORM TO THE ABOVE ADDRESS.</p>					
1. REPORT DATE (DD-MM-YYYY)		2. REPORT TYPE		3. DATES COVERED (From - To)	
01-07-2005		Technical Publication			
4. TITLE AND SUBTITLE Verification and Validation: High Charge and Energy (HZE) Transport Codes and Future Development			5a. CONTRACT NUMBER		
			5b. GRANT NUMBER		
			5c. PROGRAM ELEMENT NUMBER		
6. AUTHOR(S) Wilson, John W.; Tripathi, Ram K.; Mertens, Christopher J.; Blattnig, Steve R.; Cloudsley, Martha S.; Cucinotta, Francis A.; Tweed, John; Heinbockel, John H.; Walker, Steven A.; and Nealy, John E.			5d. PROJECT NUMBER		
			5e. TASK NUMBER		
			5f. WORK UNIT NUMBER 23-121-10-10-01		
7. PERFORMING ORGANIZATION NAME(S) AND ADDRESS(ES) NASA Langley Research Center Hampton, VA 23681-2199			8. PERFORMING ORGANIZATION REPORT NUMBER L-19150		
9. SPONSORING/MONITORING AGENCY NAME(S) AND ADDRESS(ES) National Aeronautics and Space Administration Washington, DC 20546-0001			10. SPONSOR/MONITOR'S ACRONYM(S) NASA		
			11. SPONSOR/MONITOR'S REPORT NUMBER(S) NASA/TP-2005-213784		
12. DISTRIBUTION/AVAILABILITY STATEMENT Unclassified - Unlimited Subject Category 93 Availability: NASA CASI (301) 621-0390					
13. SUPPLEMENTARY NOTES An electronic version can be found at http://ntrs.nasa.gov					
14. ABSTRACT In the present paper, we give the formalism for further developing a fully three dimensional HZETRN code using marching procedures but also development of a new code which is capable of not only validation in the space environment but also in ground based laboratories with directed beams of ions of specific energy and characterized with detailed diagnostic particle spectrometer devices. Special emphasis is given to verification of the computational procedures and validation of the resultant computational model using laboratory and spaceflight measurements. At the current state of affairs, parallel development paths for computational model implementation using marching procedures and Green's function techniques are followed as has arisen from historical demands and requirements. A new version of the HZETRN code capable of simulating HZE ions with either laboratory or space boundary conditions is under development. Validation of computational models at this time is particularly important in preparation for design of the Bush Initiative infrastructure for human exploration and demonstration of the Crew Exploration Vehicle in low Earth orbit in 2008.					
15. SUBJECT TERMS Radiation shielding methods; Space radiation; Galactic; Solar; Software					
16. SECURITY CLASSIFICATION OF:			17. LIMITATION OF ABSTRACT	18. NUMBER OF PAGES	19a. NAME OF RESPONSIBLE PERSON
a. REPORT	b. ABSTRACT	c. THIS PAGE			STI Help Desk (email: help@sti.nasa.gov)
U	U	U	UU	36	19b. TELEPHONE NUMBER (Include area code) (301) 621-0390